The Astrophysical Journal, 979:105 (18pp), 2025 February 1 https://doi.org/10.3847/1538-4357/ad9d0f

The First Exploration of the Correlations Between WISE 12 μm and CO Emission in Early-type Galaxies

Yang Gao[1,2], Enci Wang[3], Qing-Hua Tan[4], Timothy A. Davis[5], Fu-Heng Liang[6,7], Xue-Jian Jiang[8], Ning Gai[1], Qian Jiao[9], DongDong Shi[10], Shuai Feng[11,12,13], Yanke Tang[1], Shijie Li[1], and Yi-Fan Wang[1]
[1] College of Physics and Electronic Information, Dezhou University, Dezhou 253023, People's Republic of China; gao14681@mail.ustc.edu.cn
[2] International Centre of Supernovae, Yunnan Key Laboratory, Kunming 650216, People's Republic of China
[3] CAS Key Laboratory for Research in Galaxies and Cosmology, Department of Astronomy, University of Science and Technology of China, Hefei 230026, People's Republic of China; ecwang16@ustc.edu.cn
[4] Purple Mountain Observatory, Chinese Academy of Sciences, 10 Yuanhua Road, Nanjing 210023, People's Republic of China
[5] Cardiff Hub for Astrophysics Research & Technology, School of Physics & Astronomy, Cardiff University, Queens Buildings, Cardiff CF24 3AA, UK
[6] European Southern Observatory (ESO), Karl-Schwarzschild-Straße 2, 85748 Garching, Germany
[7] Subdepartment of Astrophysics, Department of Physics, University of Oxford, Denys Wilkinson Building, Keble Road, Oxford OX1 3RH, UK
[8] Research Center for Astronomical Computing, Zhejiang Laboratory, Hangzhou 311121, People's Republic of China
[9] School of Electrical and Electronic Engineering, Wuhan Polytechnic University, Wuhan 430023, People's Republic of China
[10] Center for Fundamental Physics, School of Mechanics and Optoelectric Physics, Anhui University of Science and Technology, Huainan Anhui 232001, People's Republic of China
[11] College of Physics, Hebei Normal University, 20 South Erhuan Road, Shijiazhuang 050024, People's Republic of China
[12] Guoshoujing Institute of Astronomy, Hebei Normal University, 20 South Erhuan Road, Shijiazhuang 050024, People's Republic of China
[13] Hebei Key Laboratory of Photophysics Research and Application, Shijiazhuang 050024, People's Republic of China
Received 2024 September 3; revised 2024 November 29; accepted 2024 December 8; published 2025 January 21

Abstract

We present the analysis of a comprehensive sample of 352 early-type galaxies using public data, to investigate the correlations between CO luminosities and mid-infrared luminosities observed by Wide-field Infrared Survey Explorer. We find strong correlations between both CO (1–0) and CO (2–1) luminosities and 12 μm luminosity, boasting a correlation coefficient greater than 0.9 and an intrinsic scatter smaller than 0.1 dex. The consistent slopes observed for the relationships of CO (1–0) and CO (2–1) suggest that the line ratio $R21$ lacks correlation with mid-infrared emission in early-type galaxies, which is significantly different from star-forming galaxies. Moreover, the slopes of $L_{\rm CO(1-0)}$–$L_{12\ \mu{\rm m}}$ and $L_{\rm CO(2-1)}$–$L_{12\ \mu{\rm m}}$ relations in early-type galaxies are steeper than those observed in star-forming galaxies. Given the absence of correlation with color, morphology, or specific star formation rate (sSFR), the correlation between deviations and the molecular gas mass surface density could be eliminated by correcting the possible 12 μm emission from old stars or adopting a systematically different $\alpha_{\rm CO}$. The latter, on average, is equivalent to adding a constant CO brightness density, specifically $2.8^{+0.8}_{-0.6}$ [K km s^{-1}] and $4.4^{+2.2}_{-1.4}$ [K km s^{-1}] for CO (1–0) and (2–1), respectively. These explorations will serve as useful tools for estimating the molecular gas content in gas-poor galaxies and understanding associated quenching processes.

Unified Astronomy Thesaurus concepts: Galaxy evolution (594); Interstellar medium (847); Molecular gas (1073); Infrared photometry (792); Elliptical galaxies (456)

1. Introduction

Modern galaxy formation models suggest that within dark matter halos, gas cools and collapses to form stars, a process facilitated by high gas densities and effective dust shielding from intense and hard radiation fields (R. Visser et al. 2009; M. G. Wolfire et al. 2010; M. G. Wolfire et al. 2022). Observations reveal that stars predominantly form from dusty molecular interstellar gas, as demonstrated by the strong correlation between the surface densities of the star formation rate (SFR) and molecular gas (H_2), rather than atomic gas (W. A. Baan et al. 2008; F. Bigiel et al. 2008; A. K. Leroy et al. 2008). Furthermore, a tighter correlation exists between SFRs, traced by infrared luminosity, and dense molecular gas masses, as indicated by HCN emission (Y. Gao & P. M. Solomon 2004a, 2004b).

Star formation is a multifaceted process influenced not only by the intrinsic properties of galaxies and their external environments—ranging from local to large-scale conditions (Y.-j. Peng et al. 2010; G. Kauffmann et al. 2006; C. Li et al. 2012)—but also by physical conditions on subkiloparsec scales (M. R. Krumholz & C. F. McKee 2005). To fully unravel the mechanisms driving galaxy evolution, it is crucial to explore the interplay between stars and gas across extensive and diverse samples of galaxies.

Molecular gas masses are commonly derived from the flux of ^{12}CO (hereafter CO) millimeter low-rotational (J) lines using the "conversion factor" $\alpha_{\rm CO}$ (P. M. Solomon et al. 1987; A. D. Bolatto et al. 2013). However, this conversion factor depends on several physical parameters, including metallicity, gas density, and temperature, and can vary by up to an order of magnitude (A. D. Bolatto et al. 2013; G. Accurso et al. 2017; L. J. Tacconi et al. 2020). Additionally, the size of CO samples remains significantly smaller than those of optical surveys due to sensitivity limitations and other observational uncertainties. As an alternative, gas masses can be estimated from dust masses using a metallicity-dependent gas-to-dust ratio ($\delta_{\rm GDR}$; A. K. Leroy et al. 2011; B. T. Draine & A. Li 2007). This dust-based approach accounts for not only molecular gas but also a

portion of atomic hydrogen present in the H_2-dominant molecular gas disk (C. Bertemes et al. 2018).

Building on this, we proposed that molecular gas masses for large galaxy samples can be estimated using a single mid-infrared (mid-IR) band measurement, specifically the 12 μm luminosity from the full-sky survey conducted by the Wide-field Infrared Survey Explorer (WISE; X.-J. Jiang et al. 2015; Y. Gao et al. 2019). The strong and tight correlation between CO emission and 12 μm luminosity has been established using hundreds of global galaxies and is further confirmed at subkiloparsec scales (R. Chown et al. 2021; Y. Gao et al. 2022) and in extensive galaxy samples (A. K. Leroy et al. 2023a). However, these studies include only a small number of early-type galaxies (ETGs), most of which are nondetections. Consequently, we refer to the CO (1–0) and CO (2–1) relations derived by Y. Gao et al. (2019) as representative of typical star-forming global galaxy populations.

Although the relationship between mid-IR and CO rotational line emission is among the strongest scaling relations in extragalactic astronomy (A. K. Leroy et al. 2023a), it can vary significantly across galaxies. These variations may depend on galaxy properties such as stellar mass (M_*) and specific star formation rate (SFR/M_*), potentially introducing offsets and uncertainties in molecular gas mass estimates for certain systems. Addressing this issue is critical, particularly as high-resolution and high-sensitivity interstellar medium (ISM) maps from widespread mid-IR observations, including those at high redshift, become increasingly accessible with the successful commissioning of the James Webb Space Telescope (JWST; G. H. Rieke et al. 2015). In this work, we for the first time explore this scaling relation for early-type galaxies and further investigate the dependence on galaxy properties.

The WISE 12 μm band spans wavelengths from 7.5 to 16.5 μm (T. H. Jarrett et al. 2011), capturing a blend of prominent polycyclic aromatic hydrocarbon (PAH) feature emissions (B. T. Draine & A. Li 2007) and continuum emissions from stochastically heated small dust grains (E. L. Wright et al. 2010). PAH carriers are spatially mixed to varying degrees with cold dust and molecular gas (E. Churchwell et al. 2006; G. J. Bendo et al. 2008, 2010; K. M. Sandstrom et al. 2010; K. M. Sandstrom et al. 2012). These molecules absorb ionizing ultraviolet (UV) photons from H II regions and reemit infrared radiation through features like C–H bending and C–C stretching, contributing up to 20% of a galaxy's total infrared power (J. D. T. Smith et al. 2007; A. M. Diamond-Stanic & G. H. Rieke 2010). Additionally, heating within photodissociation regions can dissipate via collisionally excited rotational–vibrational H_2 lines and rotational transitions of other abundant molecules (R. Meijerink & M. Spaans 2005). Consequently, on scales ranging from kiloparsecs to integrated galaxies, PAH emissions exhibit a strong association with molecular gas tracers such as CO (I. Cortzen et al. 2019).

The mid-IR continuum emission from dust grains primarily responds to UV radiation from young stars, though contributions from older stellar populations can dominate in some cases (A. K. Leroy et al. 2012; M. Boquien et al. 2016). Observations suggest that PAH emission is more closely correlated with molecular gas tracers such as CO than the mid-IR continuum alone (A. K. Leroy et al. 2023b; C. M. Whitcomb et al. 2023). In ETGs, where star formation is minimal or absent (S. K. Yi et al. 2005; S. Kaviraj et al. 2007), 12 μm emission from the circumstellar material heated by post-AGB stars may become significant (T. A. Davis et al. 2014), with morphology playing a key role in determining mid-IR properties (P. Temi et al. 2009). These galaxies, often rich in hot gas but with low star formation efficiency (E. O'Sullivan et al. 2001), provide a unique environment to study the relative contributions of PAH features, dust continuum, and CO-dark gas (J. Chastenet et al. 2019; A. K. Leroy et al. 2019).

Our paper is structured as follows. In Section 2, we describe the sample and data used in this paper. In Section 3, we present the results of correlations between CO and WISE 12 μm luminosities for ETGs and examine their dependence on galaxy properties. In Section 4, we attempt to explain the physical origin of the higher slope in ETGs and make two relevant preliminary tests in Appendices A and B. Finally, we summarize our findings in Section 5.

2. Sample and Data

2.1. CO Data

To maximize the sample size for studying the relationships between CO and mid-IR emission, it is essential to gather CO data for as many ETGs as possible, given the limited availability of CO observations compared to the all-sky coverage of 12 μm data. To minimize biases due to incompleteness, most of our ETGs (317 out of 352) are drawn from two volume-limited surveys: ATLAS3D (L. M. Young et al. 2011), which includes galaxies with $M_K < -21.5$ and distances <42 Mpc, and MASSIVE (C.-P. Ma et al. 2014; T. A. Davis et al. 2019), targeting galaxies within 108 Mpc and $M_K < -25.3$. To supplement this data set, we incorporate CO measurements from the statistically complete samples of nearby group E/S0 galaxies in SAURON (F. Combes et al. 2007) and group-dominant ETGs in CLoGS (E. O'Sullivan et al. 2018), along with CO (1–0) and CO (2–1) luminosities of four dwarf S0 galaxies from X. Ge et al. (2021) observed with the IRAM 30 m telescope.

For galaxies with overlapping CO measurements across these surveys, we prioritize data with higher signal-to-noise ratios (S/Ns), detections over nondetections, and stricter upper limits where applicable. In total, we obtain 82 CO (1–0) and 76 CO (2–1) detections with S/N $\geqslant$3 and use 5 times the uncertainty as upper limits for nondetections.[14] Most of the CO (1–0) and CO (2–1) intensities in our data set were measured with the IRAM 30 m telescope, but the conversion factors from intensity to flux density differ across the original referenced papers. To ensure consistency, we adopt a standard conversion factor of 4.73 Jy K^{-1} to normalize all IRAM 30 m observations at both frequencies in our sample (L. M. Young et al. 2011). Finally, we calculate the CO line luminosities in units of [K km s^{-1} pc^2] using the formula provided by A. D. Bolatto et al. (2013):

$$\left(\frac{L_{\rm CO}}{\rm K\ km\ s^{-1}\ pc^2}\right) = 2453\left(\frac{S_{\rm CO}\Delta v}{\rm Jy\ km\ s^{-1}}\right)\left(\frac{D_{\rm L}}{\rm Mpc}\right)^2(1+z)^{-1}. \quad (1)$$

2.2. WISE 12 μm Luminosity

The 12 μm luminosities in CO (1–0) and CO (2–1) beams are denoted as $L_{12\ \mu{\rm m}(1-0)}$ and $L_{12\ \mu{\rm m}(2-1)}$, as shown in Table 2.

[14] These CO nondetections include galaxies with measured fluxes less than 3 times their uncertainty (σ), even extending to negative values. Additionally, adopting different upper limits between 2σ and 5σ does not significantly alter the slopes of these scaling relations or affect subsequent conclusions.

We calculated the 12 μm luminosities based on the WISE band 3 flux and uncertainty maps downloaded from the NASA/IPAC Infrared Science Archive (WISE Team 2020), following the methodology outlined in R. Chown et al. (2021) and Y. Gao et al. (2022).

The detailed reduction process for the 12 μm data is as follows. Background maps were estimated and subtracted using the SExtractor package (E. Bertin & S. Arnouts 1996). During this step, we derived the WISE 12 μm magnitudes ($\mathrm{mag}_{12\,\mu\mathrm{m}}$) and their instrumental uncertainties for galaxies with CO measurements taken by interferometers. For galaxies observed with single-dish telescopes, the background-subtracted flux and uncertainty images were convolved to match the Gaussian point-spread function corresponding to the CO beam sizes. In 12 μm maps, the flux ($F_{12\,\mu\mathrm{m}}$) is in units of digital numbers (DNs), where 1 DN corresponds to 18.0 mag (zero-point magnitude), and zero magnitude attributes isophotal frequency equivalent flux density 31.674 Jy (S_0, T. H. Jarrett et al. 2011). The flux density in Jy is calculated as:

$$\begin{aligned} S_{12\,\mu\mathrm{m}}/Jy &= 31.674 \times 10^{-0.4\,\mathrm{mag}} \\ &= 1.998 \times 10^{-6} F_{12\,\mu\mathrm{m}}/DN. \end{aligned} \quad (2)$$

For flux density measurements within the CO beams, a correction factor of 1.133 × (beam size/pixel size)^2 was applied. The 12 μm luminosity was then computed using the formula:

$$L_{12\,\mu\mathrm{m}}/L_\odot = 4\pi D_L^2 \Delta\nu S_{12\,\mu\mathrm{m}}/\mathrm{Jy}, \quad (3)$$

where the bandwidth $\Delta\nu$ is 1.1327×10^{13} Hz in the 12 μm band. The total uncertainty in $L_{12\,\mu\mathrm{m}}$ was derived from the smoothed, background-subtracted flux and uncertainty images, incorporating instrumental uncertainty and a 4.5% zero-point uncertainty in quadrature, following a methodology similar to Appendix A of R. Chown et al. (2021).

2.3. Galaxy-integrated Parameters

The morphological T types, which classify galaxies based on spiral arm strength and ellipticity (H.-A. Pan et al. 2022), were obtained for 346 galaxies from the Two Micron All Sky Survey Photometric Redshift catalog (J. P. Huchra et al. 2012). For the remaining six targets, the classifications for NGC 7693, PGC 029321, and PGC 061468 were taken from the ATLAS3D project (M. Cappellari et al. 2011). PGC 35225 and PGC 44685 were identified as dwarf S0 galaxies based on their visual morphologies and B-band magnitudes, as discussed in X. Ge et al. (2021). The classification of NGC 2292 was sourced from G. de Vaucouleurs et al. (1991) and is available via the HyperLeda database.[15]

Additional parameters displayed in Figure 1, such as the stellar mass, color, and Sersic index, are taken from the NASA Sloan Atlas (NSA), which is a catalog of images and parameters for Sloan Digital Sky Survey (SDSS) galaxies with $z < 0.15$ (M. R. Blanton et al. 2011).

Almost all the sample galaxies have T type < 0 with only 12 exceptions, which are also identified as ETGs using high-quality imaging in ATLAS3D. This subset does not significantly affect our fitting results or conclusions. Most of these ETGs are also red, as shown in Figure 1, although the sample selection is based on morphology rather than color. For galaxies with CO (1–0 or 2–1) detections, over 77% have a Sersic index (n) $\geqslant 2$, about 75% fall within the red sequence based on their M_r and $u - r$ colors, and roughly 72% have near-UV $- r$ values greater than 4. The star formation activity in these ETGs spans a wide range, differing significantly from that in star-forming galaxies, making this sample suitable for examining whether the correlation between 12 μm and CO emission is influenced by galaxy properties.

We compute the SFR for galaxies with detected IRAS 60 and 100 μm luminosities, using the calibrations of D. B. Sanders & I. F. Mirabel (1996) and R. C. J. Kennicutt (1998), assuming the E. E. Salpeter (1955) initial mass function.

3. Results

3.1. The L_{CO}–$L_{12\,\mu m}$ Correlations in ETGs

Figure 2 shows our most basic result, a power-law (linear in logarithmic scale) correlation between the 12 μm luminosities and the detected CO luminosities in ETGs, though they are from different surveys.

We employ a Bayesian linear regression named *LinMix*[16] (B. C. Kelly 2007), to take the uncertainties in both the L_{CO} and $L_{12\,\mu\mathrm{m}}$ into account. The Spearman's correlation coefficient (r) is 0.91 and 0.92 and the intrinsic scatter is 0.09 and 0.1 dex for CO(1–0) and CO(2–1) as listed in Table 1. The tightness and correlation are almost comparable to the relation measured based on the strongest star-forming galaxies (Y. Gao et al. 2022), although the sample of ETGs is much smaller. So, assuming the galactic conversion factor $\alpha_{\mathrm{CO}} = 3.2\ M_\odot\ (\mathrm{K\ km\ s^{-1}\ pc^2})^{-1}$, the molecular gas mass in ETGs can be estimated using:

$$\begin{aligned} \log\left(\frac{M_{\mathrm{mol}}}{\mathrm{K\ km\ s^{-1}\ pc^2}}\right) &= (1.14 \pm 0.06)\log\left(\frac{L_{12\mu\mathrm{m}}}{\mathrm{L}_\odot}\right) \\ &- (1.08 \pm 0.50). \end{aligned} \quad (4)$$

3.2. Steeper CO Versus 12 μm Slopes in ETGs

In Figure 2, we find the best-fitting relations of ETGs (represented by the dark red lines) are steeper than the results (indicated by the green lines) based on the global sample of normal galaxies as performed by Y. Gao et al. (2019).

However, the relative distribution of ETGs and normal SFGs differs in the two panels. In the left panel, at the high-luminosity end, the ETGs are located in the same region indicated by the green line. However, as the luminosity decreases, they deviate significantly below this line, which suggests that as the 12 μm emission diminishes, the CO(1–0) emission weakens further. In the right panel, the deviation between the two 12 μm versus CO(2–1) correlations of ETGs and normal SFGs shows an opposite trend compared to the CO(1–0) deviation trend shown in the left panel. Thus, it seems plausible that compared to the (extrapolated) normal galaxy sample, at a given 12 μm luminosity, ETGs have lower CO(1–0) but higher CO(2–1) luminosity. This kind of difference can be naturally explained by the effects of beam size on the CO (2–1) to CO (1–0) lines ratio $R21$ (typically central enhancement; S. Sakamoto et al. 1994; Y. Yajima et al. 2021; A. K. Leroy et al. 2022). By adopting higher $R21$ in

[15] http://atlas.obs-hp.fr/hyperleda/

[16] Obtainable from the NASA IDL Astronomy User's Library: https://asd.gsfc.nasa.gov/archive/idlastro/ftp/pro/math/linmix_err.pro.

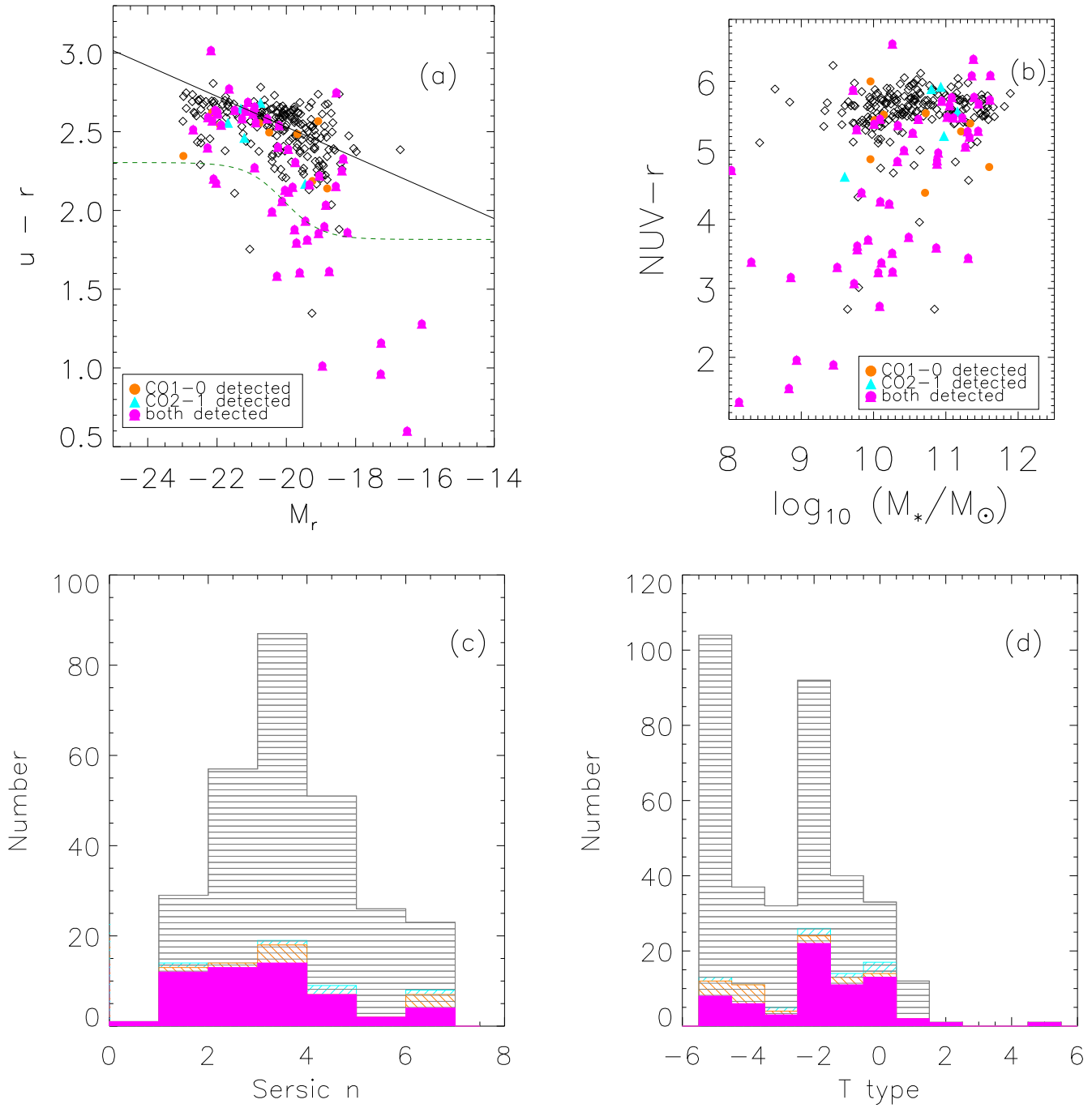

Figure 1. The panels show the distribution of our ETGs: M_r vs. $u - r$ color–magnitude diagram shown in panel a, stellar mass (M_*) vs. near-UV $- r$ plane in panel b, and Sersic index (n) in panel c. These three panels are plotted based on the data of the subsample of 274 galaxies, using SDSS photometric parameters from NSA. Panel d displays the morphological T-type distribution of the entire sample (352 galaxies). In panel a, the black line denotes the narrow early-type sequence computed by M. Cappellari et al. (2011), while the dashed line indicates the optimal divider between the red sequence and the blue cloud, as established by I. K. Baldry et al. (2004). The orange (circle), cyan (triangle), and magenta (circle + triangle) represent the detection of only CO (1–0), only CO (2–1), and both, respectively, while the black diamonds and histograms correspond to nondetections.

SFGs, we can obtain a similar trend of the deviation between ETGs and normal SFGs in the right panel as in the left panel.

So, we focus more on the fitted slope of ETGs, which is slightly higher than that of SFGs for both CO(1–0) and CO(2–1). The literature comparison presented in the left panel includes the correlations between CO(1–0) and WISE 3 band luminosity measured in Y. Gao et al. (2019), R. Chown et al. (2021), and L. Zhang & L. C. Ho (2023b). In the right panel, besides the direct linking between CO(2–1) and 12 μm luminosity, we also show the correlations between CO and PAH emission as provided by R. Chown et al. (2024) and I. Shivaei & L. A. Boogaard (2024). Notably, the detected ETGs exhibit a correlation most closely resembling that observed in the diffuse regions of nearby star-forming galaxies (outside of centers and not covered by the nebular region mask), which implies that these conditions are similar.

We directly compare the slopes of the correlations with CO(1–0) and CO(2–1) using the same sample. In particular,

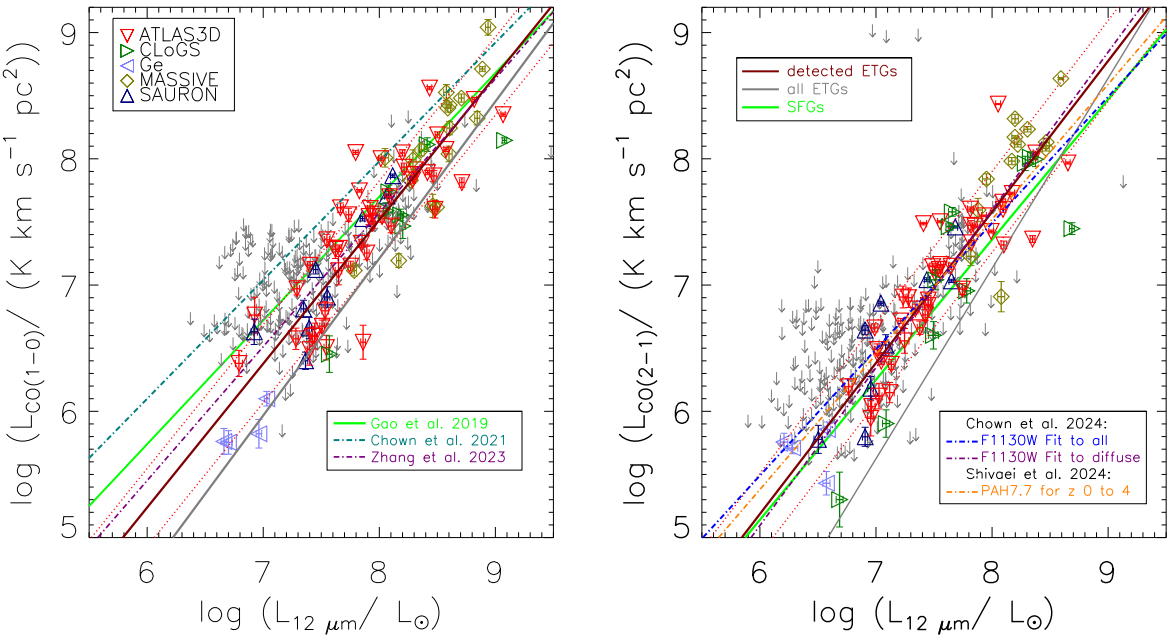

Figure 2. Correlations between the CO (1–0) and CO (2–1) luminosities and the mid-IR monochromatic luminosities ($L_{12\ \mu m}$) as measured in the WISE 12 μm band for early-type galaxies. As indicated in the upper left corner, different colors and symbols represent detections from various CO projects, with error bars showing their respective measurement uncertainties. The dark gray downward-pointing arrows mean 5σ CO upper limits. The dark red solid line and two dotted red lines, respectively, are the best-fitting linear relation (with parameters listed in Table 1) and the 1σ total/observed scatter for detections, and the gray line shows the fit when considering upper limits. In the left panel, we compile the best-fitting between $L_{12\ \mu m}$ and $L_{CO(1-0)}$ based on various samples for comparison: the green line is the global (galaxy-wide) relation (Y. Gao et al. 2019), the blue dotted–dashed line indicates the spatially resolved one in nearby star-forming galaxies (R. Chown et al. 2021), the purple line shows the spatially resolved one in nearby star-forming galaxies and low-luminosity active galactic nuclei (L. Zhang & L. C. Ho 2023a). In the right panel, we display the correlation between CO (2–1) and W3 band luminosity, and the "adjusted" correlations between CO (2–1) and PAH (F1130W and 7.7 μm) luminosity with the same slopes measured based on all pixels (blue) and diffuse regions (purple) at 50–150 pc scales in 66 nearby galaxies (R. Chown et al. 2024), and main-sequence galaxies at redshifts ranging from 0 to 4 (orange; I. Shivaei & L. A. Boogaard 2024), but offsets fitted based on our samples.

based on 68 galaxies with detected emissions in both transitions, the slopes of the relations are nearly identical, measuring 1.16 $\pm$ 0.06 for CO(1–0) and 1.16 $\pm$ 0.07 for CO(2–1). This is different from the $R_{21} \propto I_{MIR}^{0.2}$ relation statistically inferred by Y. Gao et al. (2019) and A. K. Leroy et al. (2023a), which is explained by the variation in $R21$ with the local SFR surface density in local star-forming or disk galaxies (J. S. den Brok et al. 2021; Y. Yajima et al. 2021; A. K. Leroy et al. 2022). This discrepancy may be a hint that the excitation condition of CO molecular rotational transitions is different in star-forming and early-type galaxies due to low star formation activity or indicate that the relation between 12 μm luminosity and SFR change in ETGs because the old stars can also contribute to the MIR emission.

In Figure 2, the 5σ CO upper limits for nondetections are close to the best-fitting line for detections, suggesting that these nondetections fall significantly below the fit. Consequently, including these nondetections in the analysis could substantially alter the best-fit parameters, as shown in Table 1.[17] Under similar observational depths, nondetection might signify samples with distinct physical properties (i.e., weaker CO) as our assumptions in Appendix A, and some of these nondetections may hint at special galaxy evolutions.

3.3. No Significant Influence of Global Galaxy Properties

It remains to be determined whether the slightly varying slopes observed in SFGs and ETGs would impact the efficacy of using the broadband WISE 12 μm band as a highly efficient alternative for estimating molecular gas mass. Consequently, our investigation focuses on examining how deviations correlate with representative quantities that are usually used to separate early-type and star-forming galaxies, such as the color, morphology, stellar mass, and sSFR.

Variations in these parameters, such as dust attenuation and morphology, may imply the PAH excitation (12 μm emission) is linked with different stellar populations (G. J. Bendo et al. 2020). Notably, as the sSFR declines, the prominence of IR emission originating from recent star-forming activities lessens, while the contribution of dust heating by older stellar populations becomes more significant. This kind of analysis is the unique advantage of the ETG sample, enabling the exploration of the link between the WISE 12 μm emission and molecular gas content under these specific conditions.

Based on Figure 2, we then define the parameters $\Delta\log(L_{CO(1-0)})$ and $\Delta\log(L_{CO(2-1)})$ to characterize the deviation (overestimation or underestimation) of a given galaxy from the best-fitting relation of SFGs, follow the similar method in Y. Gao et al. (2022):

$$\Delta\log(L_{CO}) \equiv \log(L_{CO,obs}) - \log(L_{CO,est}),$$
$$\log\left(\frac{L_{CO(1-0),est}}{\mathrm{K\ km\ s^{-1}\ pc^2}}\right) = 0.98\log\left(\frac{L_{12\mu m}}{L_\odot}\right) - 0.14,$$
$$\log\left(\frac{L_{CO(2-1),est}}{\mathrm{K\ km\ s^{-1}\ pc^2}}\right) = 1.11\log\left(\frac{L_{12\mu m}}{L_\odot}\right) - 1.52. \quad (5)$$

As shown in Figure 3, there is no dependence of these deviations on the global properties of the host galaxies: NUV $-$ r color, T type, or even sSFR. Consequently, the

[17] We use *LinMix* (B. C. Kelly 2007) and a new method provided by T. Jing & C. Li (2024) to do fitting and get similar results, suggesting that the differences should be from the data themselves.

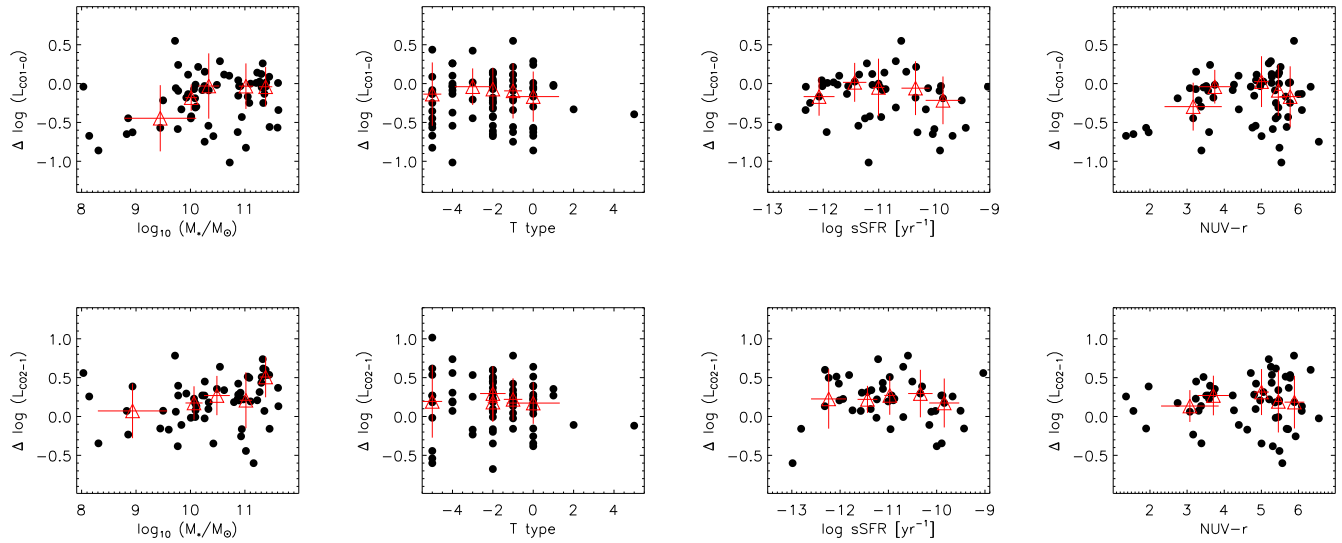

Figure 3. Scaling of $\Delta \log(L_{\rm CO})$, calculated using Equations (5) and representing the deviation from typical star-forming global $L_{\rm CO}$–$L_{12\ \mu{\rm m}}$ relations (Y. Gao et al. 2019), plotted against the basic properties of integrated galaxies. These properties include stellar mass M_*, T type, sSFR, and NUV − r color arranged from left to right. The plots show CO (1–0) in the top panels and CO (2–1) in the bottom panels. Large red triangles with error bars indicate the median and scatter for galaxies in five subsamples from left to right.

Table 1
Summary of Best-fit Relations

Data Pair (y versus x)	Number of Galaxies		k	b	Scatter		r	Figure
	Detections	Upper Limits			$\sigma_{\rm tot}$	$\sigma_{\rm int}$		
(1)	(2)	(3)	(4)	(5)	(6)	(7)	(8)	(9)
$\log(L_{\rm CO(1-0)})$ versus $\log L_{12\mu{\rm m}}$	82	0	1.14 ± 0.06	−1.59 ± 0.50	0.31	0.09	0.91 ± 0.02	Left panel in Figure 2
$\log(L_{\rm CO(1-0)})$ versus $\log L_{12\mu{\rm m}}$	82	258	1.24 ± 0.07	−2.72 ± 0.52	0.31	0.16	0.87 ± 0.02	Left panel in Figure 2
$\log(L_{\rm CO(2-1)})$ versus $\log L_{12\mu{\rm m}}$	76	0	1.19 ± 0.06	−2.00 ± 0.49	0.32	0.10	0.92 ± 0.02	Right panel in Figure 2
$\log(L_{\rm CO(2-1)})$ versus $\log L_{12\mu{\rm m}}$	76	262	1.52 ± 0.10	−4.86 ± 0.78	0.37	0.10	0.82 ± 0.02	Right panel in Figure 2
Galaxies with both CO (1–0) and (2–1) detections								
$\log(L_{\rm CO(1-0)})$ versus $\log L_{12\mu{\rm m}}$	68	0	1.16 ± 0.06	−1.72 ± 0.52	0.28	0.08	0.92 ± 0.02	...
$\log(L_{\rm CO(2-1)})$ versus $\log L_{12\mu{\rm m}}$	68	0	1.16 ± 0.07	−1.69 ± 0.54	0.32	0.10	0.92 ± 0.02	...

Note. The rows display the best-fitting linear relations of $L_{\rm CO}$[K km s^{-1} pc^{-2}] versus $L_{12\ \mu{\rm m}}$[L$_\odot$] in the logarithmic space. All relations are characterized by the equation $y = kx + b$, along with the derived intrinsic scatter $\sigma_{\rm int}$ and Spearman's correlation coefficient r provided by *LinMix* fitting.

empirical predictor presented in Y. Gao et al. (2019) remains applicable for estimating CO luminosity and molecular gas content in ETGs to study the gas-driven quenching process (E. Wang et al 2018a, 2018b, 2019), albeit with increased scatter and a systematic offset, and the offset should be corrected without any other information (as shown in Appendix B).

Only the low-mass ($M_* \leqslant 10^{10}\ M_\odot$) galaxies show a weak dependence ($r = 0.5$) of $\Delta \log(L_{\rm CO(1-0)})$ on the integrated stellar mass, which is similar to the low-mass SFGs where the presence of CO-dark molecular gas is possibly increasing (J. Kim et al. 2022). However, this dependence on the stellar mass cannot fully explain the different slopes between early-type and star-forming galaxies.

4. Discussion

4.1. Physical Origin of the Higher Slope in ETGs

The CO–mid-IR correlation is often interpreted as reflecting the relationship between molecular gas as the fuel and the resulting star formation. However, ETGs are significantly fainter than SFGs in both 12 μm and CO bands. The steeper CO–mid-IR slope observed in ETGs suggests either less CO relative to mid-IR emission or, equivalently, more mid-IR emission per unit molecular gas. If SFRs were solely estimated from 12 μm emission, this would imply paradoxically shorter molecular depletion times in ETGs compared to SFGs, a conclusion that conflicts with observational evidence (e.g., D. Colombo et al. 2018).

These excess mid-IR emissions relative to CO likely originate from processes unrelated to recent star formation or its fuel (i.e., molecular gas traced by CO). Such contributions may include "cirrus" emission from dust heated by older stellar populations (E. Donoso et al. 2012; A. Villaume et al. 2015) and the widespread presence of PAHs in diverse astrophysical environments (A. G. G. M. Tielens 2008; D. M. Hudgins & Allamandola. Allamandola 2005).

There are two potential theoretical explanations for the steeper CO–mid-IR slope observed in ETGs. First, while the deviations $\Delta \log(L_{\rm CO})$ do not correlate with sSFR, numerous studies have highlighted the significant influence of older stars

on mid-IR broadband photometry. The excitation of PAHs by older stars is particularly prominent in late-type flocculent spirals (P. Temi et al. 2009; G. J. Bendo et al. 2020; L. Zhang & L. C. Ho 2023b). To address this, we applied a methodology similar to that in T. A. Davis et al. (2023; Appendix A) to subtract the contribution of circumstellar dust around hot old stars from the 12 μm emission, recovering the correlation between 12 μm and CO (1–0) luminosities typical of star-forming galaxies. Additionally, the lack of dependence of these deviations on sSFR may arise from contamination in far-IR emission used to compute SFR, which can include contributions from mass-losing red giant stars and buoyantly transported or accreted dust (P. Temi et al. 2009), coupled with the fact that sSFR represents an integrated property rather than a local one.

The second potential interpretation is that the PAHs trace the ISM more directly (A. Li 2020), because the diffuse PAH emission typically encompasses, rather than residing within, the star-forming region containing ionized gas and hot dust (C. Watson et al. 2008). Notably, the PAH flux at the 11.3 μm band shows a strong enhancement in ETGs, which should be dominated by electronic collisions instead of stellar photons (H. Kaneda et al. 2008). As a result, PAHs in these elliptical galaxies can act as tracers for the gas present in these galaxies' harsh environments as reviewed by A. D. Bolatto et al. (2013) and A. Saintonge & B. Catinella (2022). Moreover, the lack of CO emission that effectively means higher $\alpha_{\rm CO}$ could also be explained if the fraction of molecular gas in a CO-dark phase or atomic hydrogen gas (R. A. M. Walterbos & P. B. W. Schwering 1987) is increased within regions with lower $\Sigma_{\rm H2}$. In such areas, mid-IR such as PAH emission might still be visible, even though CO is very faint (J. Chastenet et al. 2019; A. K. Leroy et al. 2023a; K. M. Sandstrom et al. 2023; C. M. Whitcomb et al. 2023). Additionally, the dark-gas fraction is insensitive to the radiation field but could be high as column densities become small (M. G. Wolfire et al. 2010). Then, we do a simple and rough attempt in Appendix B and discover the deviations could be significantly decreased, by adding a constant CO brightness density, averaging $2.8^{+0.8}_{-0.6}$ [K km s^{-1}] and $4.4^{+2.2}_{-1.4}$ [K km s^{-1}] for CO (1–0) and (2–1), respectively, which is assumed to correct the potential CO-dark gas. These findings may hint at higher $R21$ (averaging 1.57) within the regions with lower $\Sigma_{\rm mol}$, where the ratio covers a relatively wide range (J. Koda et al. 2020), or more CO (2–1) dark gas than CO (1–0) one.

We find that the CO deviation between ETGs and SFGs could diminish after applying corrections based on either of these two hypotheses. However, it is challenging to conclusively determine a preference. At the most basic level, we affirm that the ETGs resemble the CO-nondetected regions in SFGs. Practically, we make a much more powerful attempt to assess the bias in molecular gas mass estimates from 12 μm in ETGs and provide a potential method to correct this bias.

5. Summary

We conducted an initial investigation into the relationship between CO and WISE 12 μm emission in early-type galaxies. Utilizing a sample of 352 nearby ETGs, we determined the correlations between CO and 12 μm luminosities for both CO (1–0) and CO (2–1) and compared them to those from SFGs. To elucidate the differences, we then explored the deviations as functions of the host galaxy's properties and local molecular gas. Our main conclusions can be summarized as follows:

1. We confirm strong power-law correlations also exist between $L_{\rm CO}$ and $L_{12\ \mu{\rm m}}$ in early-type galaxies. Compared to the typical star-forming global (galaxy-wide) galaxies, both $L_{\rm CO(1-0)}$ versus $L_{12\ \mu{\rm m}}$ and $L_{\rm CO(2-1)}$ versus $L_{1\ 2\mu{\rm m}}$ relations in ETGs exhibit steeper slopes.
2. Based on these same detected ETGs, CO (1–0) and CO (2–1) display identical slopes in their CO versus 12 μm relations. This indicates that $R21$ remains unchanged regardless of the mid-IR emission, which is notably different from the behavior observed in SFGs.
3. For these ETGs, we compute the $L_{\rm CO}$ deviations relative to the typical best-fitting relations with $L_{12\mu{\rm m}}$ measured based on SFGs. These deviations, $\Delta\ \log(L_{\rm CO(1-0)})$ and $\Delta\ \log(L_{\rm CO(2-1)})$, show no dependence on galaxy-integrated properties such as color, sSFR, and morphology. Only ETGs with low stellar masses are significantly below the typical $L_{\rm CO(1-0)}$ versus $L_{12\ \mu{\rm m}}$ relation in SFGs.
4. The correlations between $L_{\rm CO(1-0)}$ and $L_{12\ \mu{\rm m}}$ in ETGs and SFGs can be brought into agreement by correcting the estimated 12 μm emission from circumstellar material around old stars in ETGs. We further found that the deviations in the $L_{\rm CO}$ strongly depend on molecular gas densities, essentially as evidence for a systematically different $\alpha_{\rm CO}$, which is consistent with a scenario that the mid-IR flux from atomic or CO-dark gas is increased relative to CO-bright gas in regions with lower $\Sigma_{\rm mol}$. Subsequently, we discovered that such dependencies can be eliminated, by adding a constant additional CO brightness density ($2.8^{+0.8}_{-0.6}$ [K km s^{-1}] and $4.4^{+2.2}_{-1.4}$ [K km s^{-1}] to CO (1–0) and (2–1) luminosity, respectively), which may correspond to gas not traceable by CO but potentially linked to mid-IR emission.

Given the small scatter even in these gas-poor ETGs, we contend that applying the (corrected) $L_{\rm CO}$ versus $L_{12\ \mu{\rm m}}$ relations to estimate the molecular gas content would offer significant potential advantages. Such an application could greatly enhance our analytical capabilities across all types of nearby galaxies, especially considering the rare and valuable detection of molecular gas in ETGs.

Acknowledgments

This work is supported by the International Centre of Supernovae, Yunnan Key Laboratory (Nos. 202302AN360001 and 202302AN36000103), Shandong Provincial Natural Science Foundation (ZR2023MA036), and the National Science Foundation of China (grant Nos. 12033004, 12233005, 11861131007, 11803090, 12303015, and 12003070). Y.G. receives funding from the Scientific Research Fund of Dezhou University (3012304024) and the Shandong Provincial Natural Science Foundation (ZR2024QA212). E.W. thanks the support of the Start-up Fund of the University of Science and Technology of China (No. KY2030000200). F.H.L. acknowledges support from the ESO Studentship Programme and the Scatcherd European Scholarship of the University of Oxford. N.G. thanks the Fund of Dezhou University No. 2020xjpy06. Q.J. receives Research Funding from Wuhan Polytechnic University No. 2022RZ035. D.D.S. acknowledges the National Science Foundation of Jiangsu Province (BK20231106). We are deeply grateful to Prof. Y. Gao for his invaluable guidance and suggestions about the sample and data. We extend our heartfelt thanks to Prof. Cheng Li and Mr. Tao Jing for their exceptional technical assistance throughout the data analysis process.

Funding for the NASA Sloan Atlas has been provided by the NASA Astrophysics Data Analysis Program (08-ADP08-0072) and the NSF (AST-1211644).

Funding for SDSS-III has been provided by the Alfred P. Sloan Foundation, the Participating Institutions, the National Science Foundation, and the U.S. Department of Energy. The SDSS-III website is http://www.sdss3.org.

SDSS-III is managed by the Astrophysical Research Consortium for the Participating Institutions of the SDSS-III Collaboration including the University of Arizona, the Brazilian Participation Group, the Brookhaven National Laboratory, the University of Cambridge, the University of Florida, the French Participation Group, the German Participation Group, the Instituto de Astrofisica de Canarias, the Michigan State/Notre Dame/JINA Participation Group, Johns Hopkins University, Lawrence Berkeley National Laboratory, Max Planck Institute for Astrophysics, New Mexico State University, New York University, Ohio State University, Pennsylvania State University, University of Portsmouth, Princeton University, the Spanish Participation Group, University of Tokyo, University of Utah, Vanderbilt University, University of Virginia, University of Washington, and Yale University.

Software: SExtractor (E. Bertin & S. Arnouts 1996), LinMix (B. C. Kelly 2007), IDL Astronomy user's library (W. B. Landsman 1995).

Appendix A
The Possible Old Star Emission in the WISE 12 μm Band

In this section, we aim to correct the correlation between the CO (1–0) and 12 μm luminosity in ETGs, by correcting the emission from old stars following the methodology used by T. A. Davis et al. (2014).

As shown in Figure 4, our sample of 210 CO-nondetected galaxies (represented by open black circles) shows a clear correlation $r = 0.68 \pm 0.04$ between $L_{\mu m}$ and M_* (from NSA catalog), despite a significant scatter of approximately 0.39 dex. The 62 ETGs with detected CO emissions (after matching with NSA) do not display a clear correlation and mostly lie above the average position of the CO nondetections at a given stellar mass, which may be a hint that the excess of their 12 μm emission is related to star formation. We perform a fit to

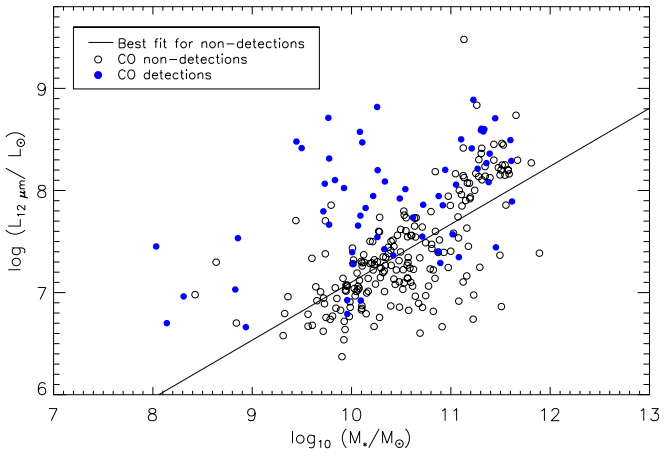

Figure 4. The WISE 12 μm luminosity within the CO(1–0) beam is plotted as a function of the stellar mass. Blue circles are ETGs with CO detection, while open circles represent those without detected molecular gas. The best fit of these nondetections is shown as a black solid line.

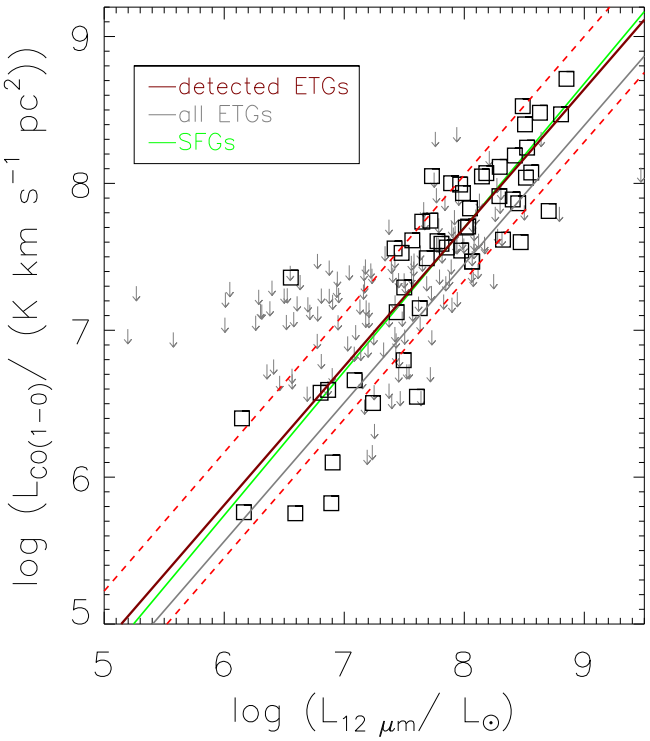

Figure 5. Same as the left panel of Figure 2, but based on the corrected 12 μm luminosity after subtracting the estimated old stars' emission.

roughly determine the mean amount of 12 μm emission caused by old stellar populations at each stellar mass. After subtracting the contributions from these older stars, 52 CO (1–0) detections and 107 nondetections have $L_{12\,\mu m}$ greater than 0. Remarkably, the correlation between corrected 12 μm and CO (1–0) luminosity closely mirrors that in SFGs,[18] as shown in Figure 5. This preliminary but convincing test suggests that the older stellar populations significantly contribute to the steeper slope we observe. Future studies will provide more detailed analyses and explore the relation for CO (2–1) in subsequent papers.

Appendix B
The Possible Components of CO-dark Gas

We plot the correlation between $\Delta \log(L_{CO})$ and molecular gas surface density (Σ_{H2}) in Figure 6, for the CO detected ETGs. Σ_{H2} is converted using galactic $\alpha_{CO} = 3.2\ M_\odot\ (\mathrm{K\,km\,s^{-1}\,pc^2})^{-1}$ and $R21 = 0.7$ from CO (1–0) and CO (2–1) brightness density, which is roughly calculated based on the beam size of the telescope for the ETGs observed with a single dish, simply assuming the gas disk fills the beam based on some sizes (T. A. Davis et al. 2013). All used CO and 12 μm luminosities and beam sizes of the ETG sample are available in Table 2.

The dependence is quite strong for both $\Delta \log(L_{CO(1-0)})$ and $\Delta \log(L_{CO(2-1)})$ in ETGs, with $r = 0.67 \pm 0.08$ (0.55 ± 0.10 after subtracting the old stars' emission such in Figure 5) and 0.68 ± 0.08, respectively, which is like and even more

[18] In SFGs, while more-evolved stellar populations can also contribute to the heating of PAH molecules (K. Ronayne et al. 2024), their contribution to the 12 μm emission is minimal, as shown by L. K. Hunt et al. (2019). For instance, the median fraction of this contribution is only about 7% in the xCOLD GASS sample.

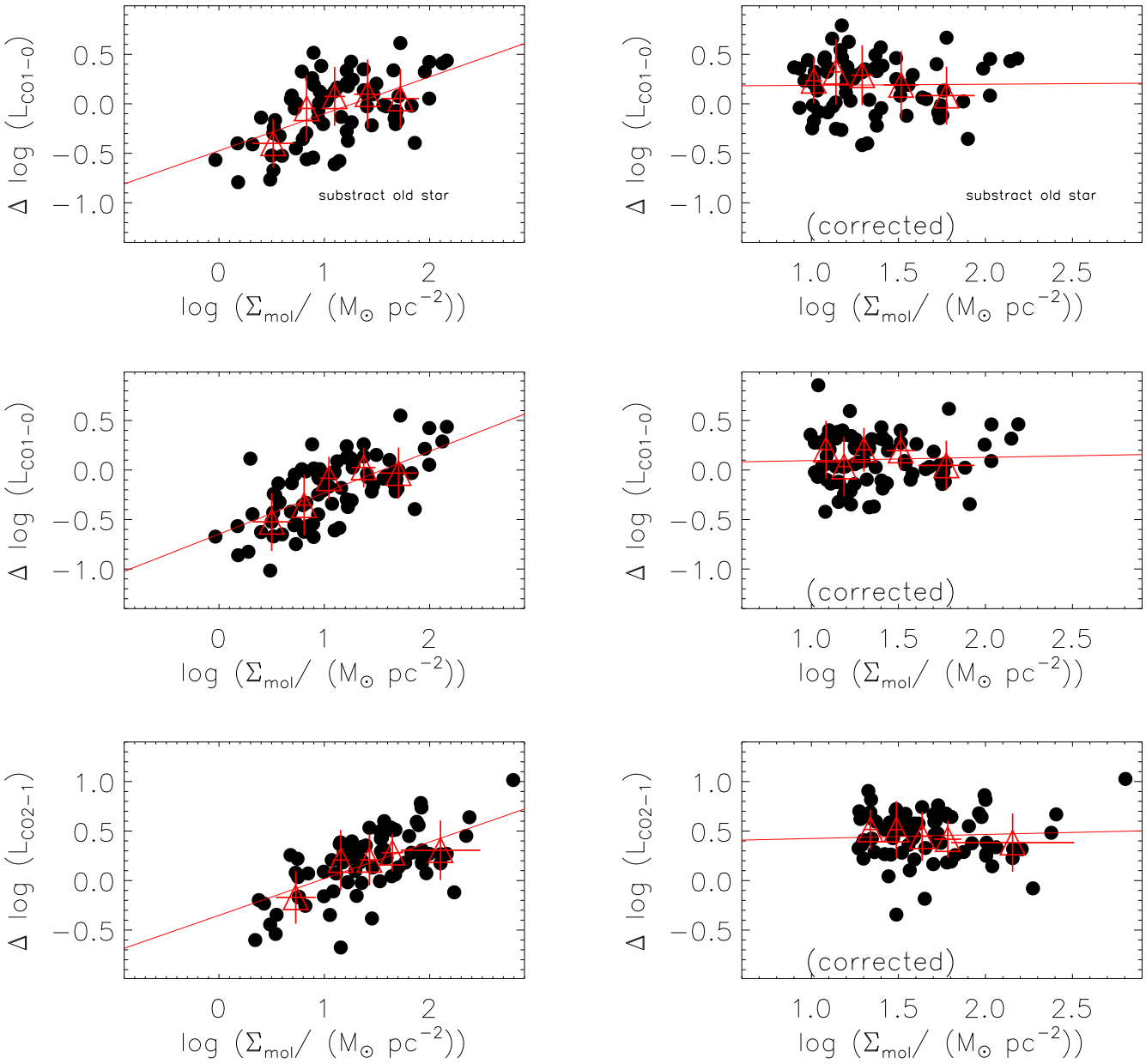

Figure 6. The left panels demonstrate the dependence of the CO luminosity deviations on molecular gas mass surface densities ($\Sigma_{\rm mol}$), which are computed based on CO (1–0) or CO (2–1) surface brightness using the galactic conversion factor $\alpha_{\rm CO} = 3.2\ M_{\odot}$ (K km s^{-1} pc^{2})$^{-1}$ and $R21 = 0.7$ (A. K. Leroy et al. 2013). The top panel is based on the correlation between CO (1–0) and 12 μm luminosities, after subtracting old stars' emission as shown in Figure 5. The right panels display the corrected correlations, by adding a constant CO brightness density, which is for CO-dark gas, in both the x- and y- axes (from top to bottom:2.2[K km s^{-1}] and 2.8[K km s^{-1}] for CO (1–0), and 4.4[K km s^{-1}] for CO (2–1)).

significant than the correlations observed in regions with very-low-molecular-gas-mass surface density in SFGs, as discussed in Y. Gao et al. (2022). The dependence on CO brightness instead of 12 μm brightness further strengthens our suspicion that the systematic higher $\alpha_{\rm CO}$ is due to the underlying CO-dark gas.

We can compute the average contribution, considering a toy assumption that these CO-dark components are statistically expected to be spatially randomly distributed, which is $2.8^{+0.8}_{-0.6}$ [K km s^{-1}] ($2.2^{+1.2}_{-0.6}$ [K km s^{-1}] for the one after subtracting the old stars' emission in Appendix A) and $4.4^{+2.2}_{-1.4}$ [K km s^{-1}] for CO (1–0) and (2–1) brightness density, respectively. These values may be unimportant in SFGs, so ETGs yield a significant chance to extract these additional CO-dark components. Besides being interpreted as a potentially higher $R21$, the higher average additional CO (2–1) background density may also suggest that the fraction of dark gas that cannot be traced by CO (2–1) exceeds that untraceable by CO (1–0), as illustrated in Figure 14 of M. Gong et al. (2020). After applying these constant brightness density corrections to the CO (1–0) and CO (2–1) luminosity, the distributions of $\Delta \log(L_{\rm CO})$ become noticeably narrow, and the dependencies on $\Sigma_{\rm H2}$ are almost eliminated, while the scatter in the correlations remains essentially unchanged.

Table 2
CO and MIR Properties of the ETG Sample Objects

Galaxy	D_L	$L_{CO(1-0)}$	$L_{12\ \mu m(1-0)}$	$ref_{(1-0)}$	$Beam_{(1-0)}$	$L_{CO(2-1)}$	$L_{12\ \mu m(2-1)}$	$ref_{(2-1)}$	$Beam_{(2-1)}$
	(Mpc)	(10^6[K km s^{-1} pc^{-2}])	($10^7 L_\odot$)		(arcsec)	(10^6[K km s^{-1} pc^{-2}])	($10^7 L_\odot$)		(arcsec)
(1)	(2)	(3)	(4)	(5)	(6)	(7)	(8)	(9)	(10)
IC0310	77.5	175.1 ± 21.3	40.28 ± 2.16	4	22	129.9 ± 5.9	16.64 ± 1.12	4	11
IC0560	27.2	<14.92	1.957 ± 0.134	1	22	<8.148	0.7445 ± 0.0725	1	11
IC0598	35.3	<33.10	2.022 ± 0.164	1	22	<9.505	0.8164 ± 0.0955	1	11
IC0676	24.6	81.89 ± 3.02	20.56 ± 0.91	1	22	29.29 ± 0.60	7.126 ± 0.347	1	11
IC0719	29.4	34.88 ± 3.63	10.56 ± 0.51	1	22	14.56 ± 0.78	3.604 ± 0.216	1	11
IC0782	36.3	<26.27	0.5824 ± 0.0849	1	22	<6.376	0.2081 ± 0.0487	1	11
IC1024	24.2	77.73 ± 2.91	25.99 ± 1.13	1	22	26.60 ± 0.68	9.820 ± 0.458	1	11
IC3631	42.0	<27.48	1.139 ± 0.139	1	22	<6.023	0.4463 ± 0.0828	1	11
NGC 0057	76.3	<50.09	16.74 ± 1.12	4	22	<32.25	6.155 ± 0.591	4	11
NGC 0227	75.9	<42.06	13.97 ± 0.98	4	22	<23.28	5.473 ± 0.546	4	11
NGC 0315	70.3	<224.2	54.53 ± 2.68	4	22	...	...	...	...
NGC 0383	71.3	335.6 ± 47.9	37.79 ± 1.98	4	22	207.7 ± 16.7	15.78 ± 1.02	4	11
NGC 0448	29.5	<17.45	2.086 ± 0.148	1	22	<4.995	0.7672 ± 0.0791	1	11
NGC 0467	75.8	98.14 ± 17.77	19.48 ± 1.24	4	22	39.31 ± 8.35	7.571 ± 0.661	4	11
NGC 0474	31.6	<14.53	2.470 ± 0.173	2	22	<5.085	0.8887 ± 0.0911	2	11
NGC 0499	69.8	<44.93	14.59 ± 0.96	4	22	<19.40	5.456 ± 0.508	4	11
NGC 0502	35.9	<23.97	2.055 ± 0.168	1	22	<5.449	0.7846 ± 0.0948	1	11
NGC 0507	69.8	<60.79	14.11 ± 0.94	4	22	<37.48	5.159 ± 0.491	4	11
NGC 0509	32.3	5.785 ± 1.880	0.8436 ± 0.0912	1	22	<2.501	0.3277 ± 0.0539	1	11
NGC 0516	34.7	<21.20	0.7449 ± 0.0911	1	22	<7.733	0.2622 ± 0.0516	1	11
NGC 0524	23.3	17.94 ± 2.20	7.805 ± 0.371	1	22	7.618 ± 0.653	2.820 ± 0.160	1	11
NGC 0525	30.7	<18.08	0.6230 ± 0.0739	1	22	<5.026	0.2320 ± 0.0430	1	11
NGC 0533	77.9	<74.56	14.54 ± 1.03	4	22	<43.11	5.175 ± 0.539	4	11
NGC 0547	74.0	<65.81	14.70 ± 1.00	4	22	<35.40	5.658 ± 0.545	4	11
NGC 0661	30.6	<17.90	2.324 ± 0.162	1	22	<5.823	0.8768 ± 0.0878	1	11
NGC 0665	74.6	252.2 ± 18.6	38.92 ± 2.07	4	22	95.94 ± 6.30	14.79 ± 1.01	4	11
NGC 0680	37.5	<23.78	5.512 ± 0.335	1	22	<7.437	2.064 ± 0.173	1	11
NGC 0708	69.0	101.8 ± 17.2	11.20 ± 0.80	4	22	...	...	...	...
NGC 0741	73.9	<57.90	15.96 ± 1.06	4	22	<37.19	5.572 ± 0.539	4	11
NGC 0770	36.7	<24.97	1.212 ± 0.124	1	22	<5.988	0.4982 ± 0.0755	1	11
NGC 0821	23.4	<10.53	2.643 ± 0.152	1	22	<1.957	0.9685 ± 0.0757	1	11
NGC 0890	55.6	<43.99	12.07 ± 0.74	4	22	<29.40	4.424 ± 0.374	4	11
NGC 0910	79.8	<34.62	11.64 ± 0.90	4	22	<24.35	4.238 ± 0.492	4	11
NGC 0936	22.4	<9.448	3.501 ± 0.186	1	22	<2.012	1.210 ± 0.085	1	11
NGC 0997	90.4	302.7 ± 22.5	50.98 ± 2.78	4	22	171.5 ± 8.5	20.20 ± 1.41	4	11
NGC 1023	10.3	<1.535	1.552 ± 0.074	2	22	<0.5374	0.5421 ± 0.0308	2	11
NGC 1060	67.4	<20.04	18.64 ± 1.12	4	22	<26.93	6.885 ± 0.570	4	11
NGC 1106	63.3	140.0 ± 6.6	119.8 ± 5.3	3	22	28.00 ± 3.00	48.72 ± 2.36	3	11
NGC 1121	35.3	<20.50	1.461 ± 0.135	1	22	<6.264	0.5991 ± 0.0808	1	11
NGC 1129	73.9	<224.2	12.71 ± 0.91	4	22	...	...	...	...
NGC 1132	97.6	<82.38	15.85 ± 1.27	4	22	<35.31	5.447 ± 0.675	4	11
NGC 1167	70.2	67.59 ± 5.73	18.54 ± 1.14	4	22	16.90 ± 2.86	6.555 ± 0.570	4	11
NGC 1222	33.3	223.7 ± 6.8	116.5 ± 4.9	1	22	92.68 ± 1.80	45.04 ± 1.97	1	11
NGC 1248	30.4	<15.42	1.607 ± 0.127	1	22	<3.773	0.5977 ± 0.0704	1	11
NGC 1266	29.9	363.3 ± 11.1	27.08 ± 1.20	1	22	271.2 ± 2.4	11.28 ± 0.54	1	11
NGC 1289	38.4	<24.42	3.155 ± 0.232	1	22	<7.349	1.193 ± 0.127	1	11

Table 2
(Continued)

Galaxy	D_L	$L_{CO(1-0)}$	$L_{12\ \mu m(1-0)}$	$ref_{(1-0)}$	$Beam_{(1-0)}$	$L_{CO(2-1)}$	$L_{12\ \mu m(2-1)}$	$ref_{(2-1)}$	$Beam_{(2-1)}$
	(Mpc)	(10^6[K km s^{-1} pc^{-2}])	($10^7 L_\odot$)		(arcsec)	(10^6[K km s^{-1} pc^{-2}])	($10^7 L_\odot$)		(arcsec)
(1)	(2)	(3)	(4)	(5)	(6)	(7)	(8)	(9)	(10)
NGC 128-H I	58.5	35.95 ± 3.78	15.25 ± 0.90	3	22	4.000 ± 1.000	3.127 ± 0.318	3	11
NGC 1453	53.5	<28.33	13.03 ± 0.76	3	22	<5.106	5.289 ± 0.423	4	11
NGC 1497	87.8	209.6 ± 25.8	69.77 ± 3.54	4	22	135.5 ± 9.9	29.28 ± 1.80	4	11
NGC 1550	52.1	<16.67	7.896 ± 0.524	3	22	<6.667	3.033 ± 0.283	3	11
NGC 1573	65.0	<38.63	12.02 ± 0.80	4	22	<20.20	4.288 ± 0.416	4	11
NGC 1600	63.8	<89.25	8.992 ± 0.651	11	15	...	...	...	...
NGC 1665	37.5	<28.52	1.664 ± 0.153	1	22	<8.050	0.5989 ± 0.0854	1	11
NGC 1684	63.5	266.9 ± 14.3	39.97 ± 2.00	4	22	148.6 ± 4.0	15.73 ± 0.96	4	11
NGC 1700	54.4	<70.89	31.62 ± 1.56	11	44	<13.09	16.36 ± 0.91	11	23
NGC 2256	79.4	<66.35	12.47 ± 0.94	4	22	<36.02	4.213 ± 0.489	4	11
NGC 2258	59.0	<51.22	12.07 ± 0.76	4	22	<15.44	4.258 ± 0.383	4	11
NGC 2274	73.8	<41.78	14.78 ± 1.00	4	22	<24.13	5.477 ± 0.534	4	11
NGC 2320	89.4	1099.9 ± 157.1	86.46 ± 4.32	13	entire	...	...	...	...
NGC 2418	74.1	<166.2	23.05 ± 1.38	11	33	...	...	...	...
NGC 2481	32.0	<19.40	3.516 ± 0.222	1	22	<7.320	1.427 ± 0.122	1	11
NGC 2513	70.8	<36.09	13.81 ± 0.93	4	22	<23.77	5.286 ± 0.506	4	11
NGC 252	71.7	129.6 ± 16.1	25.84 ± 1.48	3	22	<18.33	7.466 ± 0.627	3	11
NGC 2549	16.8	<6.196	1.628 ± 0.090	2	22	<2.161	0.6094 ± 0.0443	2	11
NGC 2563	64.4	<33.33	9.133 ± 0.664	3	22	<10.00	3.419 ± 0.362	3	11
NGC 2577	30.8	<16.21	3.644 ± 0.223	1	22	<5.196	1.460 ± 0.120	1	11
NGC 2592	25.0	<11.08	1.736 ± 0.117	1	22	<3.160	0.6774 ± 0.0639	1	11
NGC 2594	35.1	<21.62	1.103 ± 0.114	1	22	<4.618	0.4451 ± 0.0684	1	11
NGC 2672	61.5	<42.74	11.81 ± 0.77	4	22	<32.56	4.187 ± 0.392	4	11
NGC 2679	30.6	<20.71	1.202 ± 0.108	2	22	<4.768	0.4849 ± 0.0634	2	11
NGC 2685	16.7	3.754 ± 0.729	1.912 ± 0.102	1	22	<1.722	0.6218 ± 0.0448	1	11
NGC 2693	74.4	<47.25	26.06 ± 1.51	4	22	<31.26	10.31 ± 0.79	4	11
NGC 2695	23.2	<16.00	1.522 ± 0.102	2	22	<5.489	0.5785 ± 0.0549	2	11
NGC 2698	27.1	<10.12	3.188 ± 0.189	1	22	...	...	...	...
NGC 2699	23.2	<7.841	1.372 ± 0.095	2	22	<2.744	0.5255 ± 0.0518	2	11
NGC 2764	39.6	295.3 ± 10.6	65.73 ± 2.86	1	22	111.2 ± 3.9	23.72 ± 1.12	1	11
NGC 2768	21.5	8.045 ± 1.502	3.560 ± 0.186	2	22	3.352 ± 0.630	1.213 ± 0.083	2	11
NGC 2778	22.3	<9.538	0.7848 ± 0.0644	1	22	<2.977	0.2988 ± 0.0363	1	11
NGC 2783	101.4	<58.66	19.84 ± 1.51	4	22	<19.90	7.273 ± 0.824	4	11
NGC 2824	40.7	85.88 ± 6.43	16.33 ± 0.82	1	22	29.72 ± 2.54	6.585 ± 0.399	1	11
NGC 2832	105.2	<97.70	28.33 ± 1.96	4	22	<61.84	10.11 ± 1.03	4	11
NGC 2852	28.5	<15.34	1.033 ± 0.092	1	22	<4.237	0.4327 ± 0.0555	1	11
NGC 2859	27.0	<13.09	4.478 ± 0.245	1	22	<3.856	1.593 ± 0.116	1	11
NGC 2880	21.3	<8.860	1.374 ± 0.090	1	22	<3.369	0.5065 ± 0.0472	1	11
NGC 2892	101.1	<241.6	17.74 ± 1.40	4	22	...	...	...	...
NGC 2911	45.8	54.87 ± 6.62	12.07 ± 0.67	3	22	38.00 ± 3.00	4.540 ± 0.331	3	11
NGC 2950	14.5	<4.240	1.667 ± 0.087	1	22	<1.421	0.6307 ± 0.0414	1	11
NGC 2962	34.0	<22.57	4.038 ± 0.254	1	22	<11.96	1.533 ± 0.134	1	11
NGC 2974	24.3	<17.53	6.733 ± 0.330	2	22	<6.016	2.564 ± 0.152	2	11
NGC 3032	21.7	50.81 ± 1.64	11.65 ± 0.52	2	22	10.79 ± 0.31	4.471 ± 0.225	2	11
NGC 3073	32.8	6.253 ± 1.038	3.412 ± 0.220	7	22	1.407 ± 0.259	1.312 ± 0.118	7	11
NGC 3098	23.0	<9.377	1.318 ± 0.092	1	22	<2.621	0.4837 ± 0.0491	1	11

Table 2
(Continued)

Galaxy	D_L	$L_{CO(1-0)}$	$L_{12\ \mu m(1-0)}$	$ref_{(1-0)}$	$Beam_{(1-0)}$	$L_{CO(2-1)}$	$L_{12\ \mu m(2-1)}$	$ref_{(2-1)}$	$Beam_{(2-1)}$
	(Mpc)	(10^6[K km s^{-1} pc^{-2}])	($10^7 L_\odot$)		(arcsec)	(10^6[K km s^{-1} pc^{-2}])	($10^7 L_\odot$)		(arcsec)
(1)	(2)	(3)	(4)	(5)	(6)	(7)	(8)	(9)	(10)
NGC 3156	15.1	4.263 ± 0.986	0.8359 ± 0.0519	2	22	0.5995 ± 0.1532	0.3185 ± 0.0272	2	11
NGC 3158	103.4	<78.77	28.93 ± 1.96	4	22	<50.74	10.82 ± 1.05	4	11
NGC 3182	34.0	40.41 ± 4.65	8.347 ± 0.441	1	22	13.99 ± 0.89	3.074 ± 0.209	1	11
NGC3193	33.1	<25.79	5.455 ± 0.313	1	22	<5.014	2.017 ± 0.156	1	11
NGC 3226	22.9	<8.260	3.938 ± 0.207	1	22	<2.240	1.503 ± 0.100	1	11
NGC 3230	40.8	<31.73	5.077 ± 0.333	1	22	<13.81	1.875 ± 0.175	1	11
NGC 3245	20.3	3.525 ± 1.092	7.246 ± 0.336	1	22	<1.533	2.999 ± 0.158	1	11
NGC 3248	24.6	<11.29	0.9905 ± 0.0800	1	22	<4.247	0.3714 ± 0.0447	1	11
NGC 3301	22.8	<9.094	3.175 ± 0.174	1	22	<2.047	1.213 ± 0.086	1	11
NGC 3325	79.7	<56.67	7.974 ± 0.718	3	22	<20.00	2.956 ± 0.405	3	11
NGC 3377	10.7	<2.514	0.7207 ± 0.0391	2	22	<0.8767	0.2503 ± 0.0181	2	11
NGC 3379	10.7	<1.654	1.713 ± 0.081	2	22	<0.5790	0.5947 ± 0.0336	2	11
NGC 3384	10.7	<3.375	1.477 ± 0.071	2	22	<1.158	0.5449 ± 0.0315	2	11
NGC 3400	24.7	<13.62	0.5704 ± 0.0579	1	22	<2.739	0.2019 ± 0.0324	1	11
NGC 3412	11.0	<2.904	0.7157 ± 0.0394	1	22	<0.4729	0.2637 ± 0.0192	1	11
NGC 3414	20.1	<3.065	2.698 ± 0.145	2	22	<1.061	0.9522 ± 0.0675	2	11
NGC 3457	20.1	<7.115	0.8763 ± 0.0641	1	22	<1.796	0.3275 ± 0.0349	1	11
NGC 3458	30.9	<17.04	2.097 ± 0.152	1	22	<3.094	0.8116 ± 0.0847	1	11
NGC 3489	10.7	2.514 ± 0.397	2.312 ± 0.106	2	22	0.6286 ± 0.1092	0.8057 ± 0.0427	2	11
NGC 3499	26.4	<13.16	2.397 ± 0.151	1	22	<2.522	0.9017 ± 0.0792	1	11
NGC 3522	25.5	<6.047	0.4683 ± 0.0536	10	22	<2.645	0.1943 ± 0.0328	10	11
NGC 3530	31.2	<19.29		1	22	<4.314	...	1	11
NGC 3595	34.7	<21.76	2.217 ± 0.171	1	22	<4.111	0.8384 ± 0.0954	1	11
NGC 3599	19.8	<5.035	2.165 ± 0.121	1	22	1.093 ± 0.208	0.9166 ± 0.0651	1	11
NGC 3605	20.1	<9.627	0.6142 ± 0.0512	7	22	<2.113	0.2296 ± 0.0287	7	11
NGC 3607	22.2	50.07 ± 5.56	12.25 ± 0.55	6	22	14.11 ± 0.80	4.438 ± 0.225	6	11
NGC 3608	15.6	<5.347	1.077 ± 0.063	2	22	<1.231	0.3883 ± 0.0315	2	11
NGC 3610	20.8	<8.046	3.428 ± 0.178	1	22	<2.954	1.303 ± 0.085	1	11
NGC 3613	28.3	<14.38	3.815 ± 0.221	1	22	<3.410	1.354 ± 0.108	1	11
NGC 3619	26.8	36.05 ± 4.26	5.440 ± 0.285	1	22	7.944 ± 1.413	1.906 ± 0.130	1	11
NGC 3626	19.5	30.93 ± 2.91	8.815 ± 0.399	1	22	12.47 ± 0.63	3.226 ± 0.165	1	11
NGC 3630	25.0	<12.71	1.926 ± 0.126	1	22	<3.133	0.7412 ± 0.0675	1	11
NGC 3640	26.3	<12.30	4.288 ± 0.234	1	22	<2.663	1.472 ± 0.108	1	11
NGC 3641	25.9	<14.54	0.6008 ± 0.0623	1	22	<3.684	0.2435 ± 0.0374	1	11
NGC 3648	31.9	<18.87	1.888 ± 0.145	1	22	<5.500	0.7116 ± 0.0807	1	11
NGC 3658	32.7	<21.07	3.628 ± 0.230	1	22	<5.593	1.474 ± 0.126	1	11
NGC 3665	33.1	154.8 ± 8.4	31.69 ± 1.41	1	22	45.36 ± 2.66	12.37 ± 0.61	1	11
NGC 3674	33.4	<19.32	2.236 ± 0.168	1	22	<4.182	0.8509 ± 0.0929	1	11
NGC 3694	35.2	<25.92	7.179 ± 0.397	1	22	<7.831	2.979 ± 0.210	1	11
NGC 3757	22.6	<9.677	0.8331 ± 0.0673	1	22	<1.840	0.3324 ± 0.0389	1	11
NGC 3796	22.7	<10.18	0.8843 ± 0.0701	1	22	<2.022	0.3586 ± 0.0408	1	11
NGC 3805	99.4	<69.28	68.44 ± 3.65	12	31	...	...	...	...
NGC 3816	99.4	<55.04	13.36 ± 1.17	4	22	<25.50	4.847 ± 0.647	4	11
NGC 3838	23.5	<10.85	1.245 ± 0.090	1	22	<2.183	0.4923 ± 0.0504	1	11
NGC 3842	99.4	<49.05	25.91 ± 1.79	12	31	...	...	...	...
NGC 3862	99.4	41.38 ± 3.48	31.14 ± 2.02	4	22	...	...	...	...

Table 2
(Continued)

Galaxy	D_L	$L_{CO(1-0)}$	$L_{12\ \mu m(1-0)}$	$ref_{(1-0)}$	$Beam_{(1-0)}$	$L_{CO(2-1)}$	$L_{12\ \mu m(2-1)}$	$ref_{(2-1)}$	$Beam_{(2-1)}$
	(Mpc)	(10^6[K km s^{-1} pc^{-2}])	($10^7 L_\odot$)		(arcsec)	(10^6[K km s^{-1} pc^{-2}])	($10^7 L_\odot$)		(arcsec)
(1)	(2)	(3)	(4)	(5)	(6)	(7)	(8)	(9)	(10)
NGC 3941	11.9	<2.469	1.377 ± 0.069	1	22	<0.5597	0.5017 ± 0.0313	1	11
NGC 3945	23.2	<10.01	4.156 ± 0.217	1	22	<1.885	1.487 ± 0.100	1	11
NGC 3998	13.7	<3.687	5.358 ± 0.239	1	22	<0.7363	2.203 ± 0.107	1	11
NGC 4008	54.0	<26.67	7.128 ± 0.500	3	22	<10.00	2.594 ± 0.266	3	11
NGC 4026	13.2	<3.139	1.260 ± 0.067	1	22	<0.5266	0.4648 ± 0.0316	1	11
NGC 4036	24.6	<17.30	6.213 ± 0.309	1	22	6.464 ± 0.568	2.181 ± 0.136	1	11
NGC 4055	107.2	109.3 ± 15.6	39.84 ± 2.51	4	22	432.1 ± 8.6	39.17 ± 1.96	14	entire
NGC 4073	91.5	<85.19	20.04 ± 1.42	4	22	<34.89	7.077 ± 0.743	4	11
NGC 4078	38.1	<30.37	3.156 ± 0.230	1	22	<12.09	1.221 ± 0.128	1	11
NGC 410	76.7	<41.67	19.80 ± 1.26	3	22	<13.33	7.228 ± 0.648	3	11
NGC 4111	14.6	3.196 ± 0.719	3.499 ± 0.164	6	22	2.354 ± 0.217	1.354 ± 0.073	6	11
NGC 4119	16.5	14.36 ± 1.01	2.527 ± 0.128	1	22	4.578 ± 0.344	0.9752 ± 0.0608	1	11
NGC 4143	15.5	<5.013	2.409 ± 0.120	6	22	<1162.4	0.9318 ± 0.0568	6	11
NGC 4150	13.7	13.27 ± 1.07	2.831 ± 0.134	2	22	7.179 ± 0.256	1.102 ± 0.061	2	11
NGC 4168	30.9	<17.42	2.542 ± 0.174	1	22	<7.131	0.8858 ± 0.0892	1	11
NGC 4169	56.7	29.33 ± 6.62	15.92 ± 0.91	3	22	9.000 ± 2.000	6.045 ± 0.462	3	11
NGC 4179	16.5	<6.060	1.674 ± 0.091	1	22	<1.535	0.6193 ± 0.0444	1	11
NGC 4191	39.2	<27.69	3.262 ± 0.240	1	22	<5.872	1.098 ± 0.124	1	11
NGC 4203	14.7	4.722 ± 0.527	3.215 ± 0.152	6	22	<1045.5	1.227 ± 0.068	6	11
NGC 4215	31.5	<21.34	2.503 ± 0.174	1	22	<5.551	0.9534 ± 0.0947	1	11
NGC 4233	33.9	<24.51	5.407 ± 0.314	1	22	<12.26	2.129 ± 0.164	1	11
NGC 4249	38.7	<29.60	0.7002 ± 0.0980	1	22	<6.115	0.2390 ± 0.0551	1	11
NGC 4251	19.1	<4.134	2.589 ± 0.137	6	22	<2.210	0.9230 ± 0.0638	6	11
NGC 4255	31.2	<19.24	1.955 ± 0.147	1	22	<3.564	0.7618 ± 0.0826	1	11
NGC 4259	37.2	<29.60	0.7165 ± 0.0958	1	22	<11.84	0.2950 ± 0.0589	1	11
NGC 4261	31.6	<14.53	10.04 ± 0.50	2	22	<5.085	3.794 ± 0.233	2	11
NGC 4262	16.3	<3.856	1.246 ± 0.072	2	22	<1.349	0.4864 ± 0.0376	2	11
NGC 4264	37.5	<27.95	1.742 ± 0.157	1	22	<5.558	0.6213 ± 0.0869	1	11
NGC 4267	15.8	<4.556	1.273 ± 0.073	1	22	<1.567	0.4808 ± 0.0365	1	11
NGC 4268	31.7	<21.73	1.375 ± 0.119	1	22	<5.066	0.5110 ± 0.0671	1	11
NGC 4270	16.3	<3.856	0.5491 ± 0.0409	2	22	<0.6940	0.1997 ± 0.0220	2	11
NGC 4278	13.7	4.568 ± 0.892	2.486 ± 0.119	2	22	1.523 ± 0.326	0.9002 ± 0.0519	2	11
NGC 4281	24.4	<23.98	7.189 ± 0.349	1	22	<5.208	2.783 ± 0.162	1	11
NGC 4283	15.3	2.394 ± 0.571	0.6175 ± 0.0423	7	22	<0.8843	0.2320 ± 0.0227	7	11
NGC 4324	16.5	9.351 ± 1.057	1.949 ± 0.103	1	22	1.564 ± 0.229	0.5798 ± 0.0425	1	11
NGC 4339	16.0	<4.538	0.6703 ± 0.0462	1	22	<1.064	0.2366 ± 0.0240	1	11
NGC 4340	18.4	<6.867	1.032 ± 0.068	1	22	<1.825	0.3816 ± 0.0355	1	11
NGC 4342	16.5	<5.475	0.9109 ± 0.0580	1	22	<1.175	0.3725 ± 0.0321	1	11
NGC 4346	13.9	<4.200	0.9281 ± 0.0536	1	22	<0.8646	0.3507 ± 0.0272	1	11
NGC 4350	15.4	<4.852	2.190 ± 0.111	1	22	<1.203	0.8551 ± 0.0532	1	11
NGC 4365	17.9	<7.116	2.880 ± 0.146	2	22	<1.639	0.9923 ± 0.0646	2	11
NGC 4371	17.0	<6.215	1.403 ± 0.081	1	22	<2.662	0.4916 ± 0.0390	1	11
NGC 4374	16.3	<3.856	4.358 ± 0.204	2	22	<1.349	1.530 ± 0.085	2	11
NGC 4377	17.8	<5.801	1.355 ± 0.081	1	22	<1.271	0.4312 ± 0.0372	1	11
NGC 4379	15.8	<4.904	0.6206 ± 0.0433	1	22	<1.824	0.2227 ± 0.0228	1	11
NGC 4382	16.3	<5.861	3.318 ± 0.160	2	22	<2.044	1.157 ± 0.068	2	11

Table 2
(Continued)

Galaxy	D_L	$L_{CO(1-0)}$	$L_{12\ \mu m(1-0)}$	$ref_{(1-0)}$	$Beam_{(1-0)}$	$L_{CO(2-1)}$	$L_{12\ \mu m(2-1)}$	$ref_{(2-1)}$	$Beam_{(2-1)}$
	(Mpc)	(10^6[K km s^{-1} pc^{-2}])	($10^7 L_\odot$)		(arcsec)	(10^6[K km s^{-1} pc^{-2}])	($10^7 L_\odot$)		(arcsec)
(1)	(2)	(3)	(4)	(5)	(6)	(7)	(8)	(9)	(10)
NGC 4387	16.3	<5.861	0.5031 ± 0.0386	2	22	<1.349	0.1786 ± 0.0207	2	11
NGC 4406	16.8	<7.571	2.689 ± 0.135	8	22	<4.292	0.8872 ± 0.0574	8	11
NGC 4417	16.0	<5.341	1.096 ± 0.065	1	22	<1.138	0.3953 ± 0.0325	1	11
NGC 4425	16.5	<5.032	0.4629 ± 0.0370	1	22	<1.163	0.1602 ± 0.0197	1	11
NGC 4429	16.5	21.42 ± 1.57	7.004 ± 0.314	1	22	5.802 ± 0.591	2.651 ± 0.133	1	11
NGC 4434	22.4	<12.57	1.018 ± 0.076	1	22	<3.835	0.3829 ± 0.0420	1	11
NGC 4435	16.7	14.14 ± 1.26	5.667 ± 0.259	1	22	4.593 ± 0.556	2.386 ± 0.122	1	11
NGC 4442	15.3	<4.231	1.985 ± 0.102	1	22	<1.952	0.7166 ± 0.0467	1	11
NGC 4452	15.6	<4.894	0.3095 ± 0.0276	1	22	<0.9264	0.1040 ± 0.0148	1	11
NGC 4458	16.3	<5.861	0.3787 ± 0.0324	2	22	<2.044	0.1391 ± 0.0180	2	11
NGC 4459	16.3	33.62 ± 1.48	7.167 ± 0.321	2	22	11.03 ± 0.39	2.740 ± 0.136	2	11
NGC 4461	16.5	<5.048	1.271 ± 0.074	1	22	<1.578	0.4677 ± 0.0370	1	11
NGC 4472	17.1	<5.608	5.214 ± 0.242	1	22	<1.772	1.712 ± 0.094	1	11
NGC 4473	16.3	<3.856	2.434 ± 0.123	2	22	<0.6940	0.8854 ± 0.0563	2	11
NGC 4474	15.6	<4.653	0.6562 ± 0.0446	1	22	<1.704	0.2430 ± 0.0237	1	11
NGC 4476	17.6	22.84 ± 2.28	3.536 ± 0.177	9	17.55	...	...	...	...
NGC 4477	16.3	6.478 ± 1.018	2.224 ± 0.114	2	22	4.395 ± 0.362	0.8049 ± 0.0526	2	11
NGC 4478	17.0	<6.097	1.157 ± 0.070	1	22	<1.583	0.4039 ± 0.0345	1	11
NGC 4483	16.7	<5.090	0.4783 ± 0.0381	1	22	<0.9158	0.1754 ± 0.0209	1	11
NGC 4486	16.7	13.03 ± 1.26	6.088 ± 0.277	4	22	<0.6940	1.966 ± 0.103	2	11
NGC 4489	15.4	<4.466	0.3452 ± 0.0292	1	22	<1.485	0.1257 ± 0.0162	1	11
NGC 4494	16.6	<5.589	2.842 ± 0.141	1	22	<1.473	1.078 ± 0.066	1	11
NGC 4503	16.5	<5.269	1.158 ± 0.069	1	22	<1.017	0.4190 ± 0.0345	1	11
NGC 4521	39.7	<29.40	6.283 ± 0.380	1	22	<7.832	2.522 ± 0.204	1	11
NGC 4526	16.3	73.41 ± 2.34	13.04 ± 0.56	2	22	28.84 ± 0.56	4.821 ± 0.223	2	11
NGC 4528	15.8	<4.512	0.7315 ± 0.0486	1	22	<1.059	0.2785 ± 0.0261	1	11
NGC 4546	16.3	<3.856	2.926 ± 0.144	2	22	<1.349	1.100 ± 0.066	2	11
NGC 4550	15.5	<5.529	0.9541 ± 0.0580	1	22	<1.993	0.3621 ± 0.0301	1	11
NGC 4551	16.1	<5.589	0.5709 ± 0.0417	1	22	<1.864	0.2001 ± 0.0219	1	11
NGC 4552	16.3	<5.861	3.468 ± 0.167	2	22	<1.349	1.233 ± 0.072	2	11
NGC 4564	15.8	<5.615	1.391 ± 0.078	1	22	<1.803	0.5189 ± 0.0384	1	11
NGC 4570	16.3	<7.866	1.770 ± 0.095	2	22	<2.044	0.6667 ± 0.0462	2	11
NGC 4578	16.3	<4.988	0.7295 ± 0.0494	1	22	<2.154	0.2701 ± 0.0262	1	11
NGC 4596	16.5	3.943 ± 0.930	2.773 ± 0.138	1	22	1.319 ± 0.309	1.061 ± 0.065	1	11
NGC 4608	16.5	<6.345	0.9470 ± 0.0596	1	22	<1.420	0.3331 ± 0.0300	1	11
NGC 4612	16.6	<5.013	0.8249 ± 0.0543	1	22	<1.325	0.3040 ± 0.0285	1	11
NGC 4621	14.9	<4.335	2.360 ± 0.117	1	22	<0.6452	0.8445 ± 0.0518	1	11
NGC 4623	17.4	<5.173	0.4008 ± 0.0353	1	22	<1.271	0.1424 ± 0.0194	1	11
NGC 4624	16.5	<6.329	1.379 ± 0.079	1	22	<2.583	0.4647 ± 0.0368	1	11
NGC 4636	13.6	<0.7883	1.456 ± 0.076	3	22	0.200 ± 0.060	0.4858 ± 0.0332	3	11
NGC 4638	17.5	<6.354	1.572 ± 0.089	1	22	<1.486	0.5799 ± 0.0443	1	11
NGC 4643	16.5	<7.611	2.475 ± 0.125	1	22	0.8790 ± 0.2816	0.9005 ± 0.0574	1	11
NGC 4649	16.5	15.62 ± 1.95	14.71 ± 0.63	11	55	<3.092	1.788 ± 0.098	1	11
NGC 4660	15.0	<4.982	1.357 ± 0.074	1	22	<1.707	0.5224 ± 0.0372	1	11
NGC 4684	13.1	3.080 ± 0.876	2.516 ± 0.119	1	22	3.086 ± 0.318	1.028 ± 0.056	1	11
NGC 4690	40.2	<32.87	1.852 ± 0.173	1	22	<7.678	0.7318 ± 0.1015	1	11

Table 2
(Continued)

Galaxy	D_L	$L_{CO(1-0)}$	$L_{12\ \mu m(1-0)}$	$ref_{(1-0)}$	$Beam_{(1-0)}$	$L_{CO(2-1)}$	$L_{12\ \mu m(2-1)}$	$ref_{(2-1)}$	$Beam_{(2-1)}$
	(Mpc)	(10^6[K km s^{-1} pc^{-2}])	($10^7 L_\odot$)		(arcsec)	(10^6[K km s^{-1} pc^{-2}])	($10^7 L_\odot$)		(arcsec)
(1)	(2)	(3)	(4)	(5)	(6)	(7)	(8)	(9)	(10)
NGC 4694	16.5	19.56 ± 1.18	4.527 ± 0.211	1	22	5.195 ± 0.238	1.634 ± 0.090	1	11
NGC 4697	11.4	<2.304	1.786 ± 0.085	1	22	<0.5079	0.6482 ± 0.0371	1	11
NGC 4710	16.5	100.3 ± 2.9	10.31 ± 0.45	1	22	31.75 ± 0.61	3.561 ± 0.171	1	11
NGC 4733	14.5	<6.098	0.2358 ± 0.0222	1	22	<0.9409	0.079 ± 0.012	1	11
NGC 4753	22.9	68.08 ± 4.14	19.37 ± 0.85	1	22	21.64 ± 0.88	6.642 ± 0.320	1	11
NGC 4754	16.1	<4.806	1.760 ± 0.094	1	22	<1.028	0.6063 ± 0.0430	1	11
NGC 4762	22.6	<9.529	2.704 ± 0.153	1	22	<3.837	0.9407 ± 0.0725	1	11
NGC 4803	39.4	<30.40	1.187 ± 0.132	1	22	<6.631	0.4531 ± 0.0772	1	11
NGC 4839	102.0	<118.5	13.34 ± 1.18	4	22	<113.3	4.687 ± 0.649	4	11
NGC 4874	102.0	<92.78	15.70 ± 1.31	4	22	<58.16	5.422 ± 0.703	4	11
NGC 4889	102.0	<108.8	27.92 ± 1.90	4	22	<46.45	10.13 ± 1.00	4	11
NGC 4914	74.5	<42.20	17.16 ± 1.12	4	22	<19.90	6.316 ± 0.584	4	11
NGC 4956	70.9	<26.67	15.29 ± 1.00	3	22	<8.333	5.406 ± 0.512	3	11
NGC 5103	23.4	<12.19	1.114 ± 0.083	1	22	<2.267	0.4359 ± 0.0467	1	11
NGC 5173	38.4	36.58 ± 4.94	8.829 ± 0.485	1	22	13.32 ± 0.98	3.497 ± 0.247	1	11
NGC 5198	36.3	<19.16	3.076 ± 0.219	2	22	<3.448	1.098 ± 0.116	2	11
NGC 5208	105.0	514.8 ± 21.7	77.27 ± 4.11	4	22	121.1 ± 6.0	29.06 ± 1.98	4	11
NGC 5252	103.8	<128.3	301.5 ± 13.5	4	22	<74.12	134.9 ± 6.5	4	11
NGC 5273	16.1	3.926 ± 0.681	2.662 ± 0.132	1	22	2.493 ± 0.153	1.111 ± 0.066	1	11
NGC 5308	28.3	<17.70	2.971 ± 0.183	2	22	<8.151	1.072 ± 0.093	2	11
NGC 5322	30.3	<18.20	8.741 ± 0.440	1	22	<5.056	3.204 ± 0.201	1	11
NGC 5342	35.5	<19.41	1.154 ± 0.117	1	22	<4.798	0.3970 ± 0.0647	1	11
NGC 5353	35.4	38.79 ± 5.68	11.41 ± 0.58	3	22	29.00 ± 2.00	4.268 ± 0.270	3	11
NGC 5355	37.1	<27.44	2.729 ± 0.205	1	22	<11.74	1.142 ± 0.120	1	11
NGC 5358	38.0	<26.60	0.5882 ± 0.0864	1	22	<7.658	0.2490 ± 0.0545	1	11
NGC 5379	30.0	40.95 ± 3.61	4.626 ± 0.263	1	22	8.042 ± 1.595	1.713 ± 0.130	1	11
NGC 5422	30.8	<19.24	2.831 ± 0.186	1	22	<8.656	1.082 ± 0.100	1	11
NGC 5444	60.5	<23.33	10.04 ± 0.68	3	22	<10.00	3.787 ± 0.364	3	11
NGC 5473	33.2	<22.36	5.737 ± 0.325	1	22	<7.639	2.256 ± 0.167	1	11
NGC 5475	28.6	<16.78	1.979 ± 0.139	1	22	<4.564	0.7641 ± 0.0766	1	11
NGC 5481	25.8	<12.57	0.9325 ± 0.0797	1	22	<4.362	0.3450 ± 0.0447	1	11
NGC 5485	25.2	<12.62	3.280 ± 0.186	1	22	<2.934	1.108 ± 0.087	1	11
NGC 5490	71.9	<23.33	13.69 ± 0.93	3	22	<11.67	5.255 ± 0.509	3	11
NGC 5493	38.8	<30.36	7.779 ± 0.442	1	22	<8.071	2.942 ± 0.222	1	11
NGC 5500	31.7	<21.20	0.5231 ± 0.0679	1	22	<6.249	0.1914 ± 0.0396	1	11
NGC 5507	28.5	<15.77	2.001 ± 0.140	1	22	<2.915	0.7708 ± 0.0769	1	11
NGC 5557	38.8	<26.25	7.055 ± 0.410	1	22	<5.206	2.573 ± 0.204	1	11
NGC 5574	23.2	<10.23	1.064 ± 0.080	1	22	<2.252	0.3728 ± 0.0425	1	11
NGC 5576	24.8	<12.65	3.627 ± 0.200	1	22	<2.431	1.364 ± 0.098	1	11
NGC 5582	27.7	<14.98	1.554 ± 0.116	1	22	<3.055	0.5830 ± 0.0637	1	11
NGC 5611	24.5	<11.79	1.024 ± 0.081	1	22	<3.079	0.4118 ± 0.0471	1	11
NGC 5629	67.7	<33.33	8.618 ± 0.660	3	22	<15.00	3.221 ± 0.364	3	11
NGC 5631	27.0	<15.13	3.978 ± 0.223	1	22	<3.612	1.384 ± 0.105	1	11
NGC 5638	25.6	<12.61	2.212 ± 0.140	1	22	<2.390	0.7796 ± 0.0708	1	11
NGC 5687	27.2	<13.89	1.667 ± 0.120	1	22	<2.806	0.6362 ± 0.0660	1	11
NGC 5770	18.5	<6.902	0.7397 ± 0.0540	1	22	<1.517	0.2796 ± 0.0297	1	11

Table 2
(Continued)

Galaxy	D_L (Mpc)	$L_{CO(1-0)}$ (10^6[K km s^{-1} pc^{-2}])	$L_{12\ \mu m(1-0)}$ ($10^7 L_\odot$)	$ref_{(1-0)}$	$Beam_{(1-0)}$ (arcsec)	$L_{CO(2-1)}$ (10^6[K km s^{-1} pc^{-2}])	$L_{12\ \mu m(2-1)}$ ($10^7 L_\odot$)	$ref_{(2-1)}$	$Beam_{(2-1)}$ (arcsec)
(1)	(2)	(3)	(4)	(5)	(6)	(7)	(8)	(9)	(10)
NGC 5813	29.9	<3.333	4.283 ± 0.248	3	22	<5.327	1.148 ± 0.092	2	11
NGC 5831	22.8	<15.41	1.689 ± 0.108	2	22	<4.003	0.6169 ± 0.0561	2	11
NGC 5838	18.7	<7.731	4.388 ± 0.212	2	22	<2.696	1.755 ± 0.100	2	11
NGC 5839	22.0	<7.567	1.059 ± 0.077	1	22	<1.526	0.3899 ± 0.0416	1	11
NGC 584	18.7	<3.333	2.839 ± 0.147	3	22	<0.8333	1.026 ± 0.068	3	11
NGC 5845	21.8	<6.892	1.922 ± 0.116	2	22	<1.241	0.8068 ± 0.0639	2	11
NGC 5846	23.1	2.838 ± 0.946	3.716 ± 0.198	3	22	0.8000 ± 0.2000	1.222 ± 0.087	3	11
NGC 5854	26.2	<12.53	1.850 ± 0.126	1	22	<2.244	0.6632 ± 0.0656	1	11
NGC 5864	29.0	<17.30	1.848 ± 0.134	1	22	<4.387	0.6256 ± 0.0691	1	11
NGC 5866	14.9	55.77 ± 1.34	6.736 ± 0.299	6	22	<1074.2	2.309 ± 0.114	6	11
NGC 5869	24.9	<13.55	1.704 ± 0.115	1	22	<2.856	0.6335 ± 0.0612	1	11
NGC 5982	41.9	<13.25	8.307 ± 0.481	2	22	<4.587	3.074 ± 0.241	2	11
NGC 6010	30.6	<19.16	2.782 ± 0.184	1	22	<3.701	1.063 ± 0.099	1	11
NGC 6014	35.8	111.5 ± 6.4	15.80 ± 0.76	1	22	39.97 ± 1.54	6.496 ± 0.370	1	11
NGC 6017	29.0	<16.96	5.047 ± 0.277	1	22	<3.458	2.170 ± 0.149	1	11
NGC 6149	37.2	<25.09	2.347 ± 0.187	1	22	<7.118	0.9489 ± 0.1088	1	11
NGC 6278	42.9	<30.70	5.402 ± 0.357	1	22	<8.958	2.143 ± 0.196	1	11
NGC 6482	61.4	<24.14	17.57 ± 1.02	4	22	<7.198	6.504 ± 0.513	4	11
NGC 6547	40.8	<32.12	3.621 ± 0.264	1	22	<10.11	1.441 ± 0.149	1	11
NGC 6548	33.6	<24.89	3.779 ± 0.240	2	22	<17.19	1.403 ± 0.125	2	11
NGC 6658	64.0	<25.00	7.522 ± 0.581	3	22	<8.333	2.944 ± 0.330	3	11
NGC 6703	25.9	<13.41	3.040 ± 0.178	1	22	<5.487	1.122 ± 0.089	1	11
NGC 6798	37.5	13.00 ± 3.35	4.447 ± 0.287	1	22	<4.168	1.550 ± 0.145	1	11
NGC 7052	69.3	42.43 ± 8.93	28.87 ± 1.58	4	22	8.094 ± 2.233	11.99 ± 0.83	4	11
NGC 7265	82.8	<69.30	18.12 ± 1.24	4	22	<46.32	6.635 ± 0.656	4	11
NGC 7274	82.8	<45.43	13.16 ± 1.00	4	22	<13.61	4.833 ± 0.547	4	11
NGC 7280	23.7	<9.728	1.968 ± 0.124	1	22	<2.228	0.7734 ± 0.0664	1	11
NGC 7332	22.4	<8.253	3.178 ± 0.172	1	22	<1.888	1.206 ± 0.085	1	11
NGC 7454	23.2	<7.821	0.9216 ± 0.0732	1	22	<2.119	0.3375 ± 0.0402	1	11
NGC 7457	12.9	<2.892	0.4349 ± 0.0298	1	22	<0.6553	0.1503 ± 0.0153	1	11
NGC 7465	29.3	118.6 ± 4.5	37.54 ± 1.63	1	22	53.19 ± 1.19	14.89 ± 0.69	1	11
NGC 7550	72.7	117.5 ± 12.5	22.97 ± 1.36	4	22	69.19 ± 6.66	8.950 ± 0.711	4	11
NGC 7556	103.0	<51.24	17.81 ± 1.43	4	22	<21.15	5.575 ± 0.722	4	11
NGC 7618	76.3	<43.29	14.75 ± 1.02	4	22	<27.45	5.592 ± 0.554	4	11
NGC 7619	54.3	<10.00	14.21 ± 0.82	3	22	<6.667	5.279 ± 0.411	3	11
NGC 7626	54.0	<42.91	11.79 ± 0.71	4	22	...	...	...	...
NGC 7693	35.4	<23.31	0.5464 ± 0.0797	1	22	<5.663	0.2048 ± 0.0468	1	11
NGC 7710	34.0	<19.89	1.026 ± 0.107	1	22	<5.896	0.3960 ± 0.0626	1	11
NGC 924	63.6	<37.84	8.783 ± 0.641	3	22	11.00 ± 2.00	3.269 ± 0.349	3	11
NGC 978	68.7	<25.00	11.88 ± 0.83	3	22	<6.667	4.409 ± 0.443	3	11
PGC 016060	37.8	34.96 ± 5.26	8.130 ± 0.452	1	22	6.897 ± 1.507	2.814 ± 0.212	1	11
PGC 028887	41.0	<33.80	0.6769 ± 0.1023	1	22	<15.68	0.3158 ± 0.0671	1	11
PGC 029321	40.9	64.85 ± 5.52	51.44 ± 2.28	1	22	23.15 ± 1.44	22.33 ± 1.07	1	11
PGC 035754	39.0	<25.19	0.8113 ± 0.1057	1	22	<7.912	0.3358 ± 0.0653	1	11
PGC 042549	40.7	<37.35	3.980 ± 0.281	1	22	<7.100	1.455 ± 0.150	1	11
PGC 044433	40.1	<30.65	1.154 ± 0.132	1	22	<7.687	0.4815 ± 0.0810	1	11

Table 2
(Continued)

Galaxy	D_L	$L_{CO(1-0)}$	$L_{12\ \mu m(1-0)}$	$ref_{(1-0)}$	$Beam_{(1-0)}$	$L_{CO(2-1)}$	$L_{12\ \mu m(2-1)}$	$ref_{(2-1)}$	$Beam_{(2-1)}$
	(Mpc)	(10^6[K km s^{-1} pc^{-2}])	($10^7 L_\odot$)		(arcsec)	(10^6[K km s^{-1} pc^{-2}])	($10^7 L_\odot$)		(arcsec)
(1)	(2)	(3)	(4)	(5)	(6)	(7)	(8)	(9)	(10)
PGC 050395	37.2	<23.65	0.7030 ± 0.0927	1	22	<5.509	0.2787 ± 0.0563	1	11
PGC 051753	38.3	<26.26	0.7777 ± 0.1008	1	22	<6.692	0.3041 ± 0.0607	1	11
PGC 054452	29.5	<16.94	0.4181 ± 0.0570	1	22	<4.653	0.1550 ± 0.0335	1	11
PGC 056772	39.5	29.38 ± 3.65	12.64 ± 0.65	1	22	9.290 ± 0.920	5.557 ± 0.347	1	11
PGC 058114	23.8	75.22 ± 2.96	19.89 ± 0.87	1	22	35.37 ± 0.52	8.522 ± 0.402	1	11
PGC 061468	36.2	19.19 ± 3.21	4.194 ± 0.270	1	22	3.614 ± 0.815	1.761 ± 0.153	1	11
PGC 071531	30.4	<14.07	0.6711 ± 0.0762	1	22	<2.766	0.2631 ± 0.0454	1	11
PGC 170172	37.1	<29.84	0.7494 ± 0.0973	1	22	<7.520	0.3047 ± 0.0595	1	11
PGC 32543	9.1	0.5771 ± 0.1367	0.4585 ± 0.0256	5	22	0.5714 ± 0.0910	0.1613 ± 0.0122	5	11
PGC 35225	14.8	0.5672 ± 0.1215	0.5018 ± 0.0360	5	22	0.5126 ± 0.0540	0.1912 ± 0.0198	5	11
PGC 36686	10.7	1.258 ± 0.168	1.073 ± 0.054	5	22	0.7191 ± 0.0977	0.3814 ± 0.0242	5	11
PGC 44685	12.5	0.6644 ± 0.1733	0.9176 ± 0.0506	5	22	0.2693 ± 0.0577	0.3740 ± 0.0264	5	11
UGC 03960	33.2	<20.37	0.4658 ± 0.0689	1	22	<7.703	0.1541 ± 0.0382	1	11
UGC 04551	28.0	<13.31	1.822 ± 0.130	1	22	<5.707	0.7384 ± 0.0739	1	11
UGC 05408	45.8	39.82 ± 6.32	30.13 ± 1.43	1	22	20.78 ± 1.47	12.63 ± 0.69	1	11
UGC 06062	38.7	<27.33	1.664 ± 0.158	1	22	<7.965	0.6009 ± 0.0882	1	11
UGC 06176	40.1	73.23 ± 7.10	29.57 ± 1.37	1	22	39.73 ± 2.13	12.42 ± 0.65	1	11
UGC 08876	33.9	<19.97	1.184 ± 0.114	1	22	<5.110	0.4672 ± 0.0675	1	11
UGC 09519	27.6	112.1 ± 3.9	6.247 ± 0.322	1	22	30.67 ± 0.72	2.562 ± 0.162	1	11
ESO 507-25	45.2	...	...	...	...	92.00 ± 12.00	19.32 ± 0.97	3	27
NGC 1395	22.4	...	...	...	...	<10.00	5.800 ± 0.283	3	27
NGC 1779	44.4	...	...	...	...	99.00 ± 13.00	23.65 ± 1.15	3	27
NGC 2292	29.6	...	...	...	...	<16.67	2.536 ± 0.169	3	27
NGC 3078	32.7	...	...	...	...	<8.333	9.806 ± 0.496	3	27
NGC 3923	21.3	...	...	...	...	<10.00	5.812 ± 0.280	3	27
NGC 5061	28.3	...	...	...	...	<15.00	10.55 ± 0.51	3	27
NGC 5084	24.1	...	...	...	...	<5.000	8.752 ± 0.413	3	27
NGC 5153	60.5	...	...	...	...	<63.33	9.002 ± 0.631	3	27
NGC 5903	31.5	...	...	...	...	<21.67	4.675 ± 0.272	3	27
NGC 7377	46.7	...	...	...	...	103.0 ± 10.0	21.36 ± 1.07	3	27

Note. (1) Object name, (2) galaxy distance, (3) CO(1–0) luminosity (and uncertainty) from the paper referenced in Column (5), (4) WISE 12 μm luminosity in CO(1–0) beams listed in Column (6). Columns (7)–(10) are as Columns (3)–(6), but for the CO(2–1) line observations.

References. (1) L. M. Young et al. (2011), (2) F. Combes et al. (2007), (3) E. O'Sullivan et al. (2018), (4) observations of MASSIVE galaxies with IRAM (T. A. Davis & M. Bureau 2016; T. A. Davis et al. 2019; B. Ocaña Flaquer et al. 2010; E. O'Sullivan et al. 2015; T. Wiklind et al. 1995), (5) X. Ge et al. (2021), (6) G. A. Welch & L. J. Sage (2003), (7) L. J. Sage et al. (2007), (8) T. Wiklind et al. (1995), (9) L. M. Young (2002), (10) G. A. Welch et al. (2010), (11) A. Georgakakis et al. (2001), (12) G. R. Knapp & M. P. Rupen (1996), (13) L. M. Young (2005), (14) provided by Davis privately.

ORCID iDs

Yang Gao https://orcid.org/0000-0002-2851-886X
Enci Wang https://orcid.org/0000-0003-1588-9394
Qing-Hua Tan https://orcid.org/0000-0003-3032-0948
Timothy A. Davis https://orcid.org/0000-0003-4932-9379
Fu-Heng Liang https://orcid.org/0000-0003-2496-1247
Ning Gai https://orcid.org/0000-0002-9308-587X
Qian Jiao https://orcid.org/0000-0002-4895-9208
DongDong Shi https://orcid.org/0000-0002-3264-819X
Shuai Feng https://orcid.org/0000-0002-9767-9237
Yanke Tang https://orcid.org/0000-0003-4207-1694

References

Accurso, G., Saintonge, A., Catinella, B., et al. 2017, MNRAS, 470, 4750
Baan, W. A., Henkel, C., Loenen, A. F., Baudry, A., & Wiklind, T. 2008, A&A, 477, 747
Baldry, I. K., Glazebrook, K., Brinkmann, J., et al. 2004, ApJ, 600, 681
Bendo, G. J., Lu, N., & Zijlstra, A. 2020, MNRAS, 496, 1393
Bendo, G. J., Draine, B. T., Engelbracht, C. W., et al. 2008, MNRAS, 389, 629
Bendo, G. J., Wilson, C. D., Warren, B. E., et al. 2010, MNRAS, 402, 1409
Bertemes, C., Wuyts, S., Lutz, D., et al. 2018, MNRAS, 478, 1442
Bertin, E., & Arnouts, S. 1996, A&AS, 117, 393
Bigiel, F., Leroy, A., Walter, F., et al. 2008, AJ, 136, 2846
Blanton, M. R., Kazin, E., Muna, D., Weaver, B. A., & Price-Whelan, A. 2011, AJ, 142, 31
Bolatto, A. D., Wolfire, M., & Leroy, A. K. 2013, ARA&A, 51, 207
Boquien, M., Kennicutt, R., Calzetti, D., et al. 2016, A&A, 591, A6
Cappellari, M., Emsellem, E., Krajnović, D., et al. 2011, MNRAS, 413, 813
Chastenet, J., Sandstrom, K., Chiang, I.-D., et al. 2019, ApJ, 876, 62
Chown, R., Li, C., Parker, L., et al. 2021, MNRAS, 500, 1261
Chown, R., Leroy, A. K., Sandstrom, K., et al. 2024, arXiv:2410.05397
Churchwell, E., Povich, M. S., Allen, D., et al. 2006, ApJ, 649, 759
Colombo, D., Kalinova, V., Utomo, D., et al. 2018, MNRAS, 475, 1791
Combes, F., Young, L. M., & Bureau, M. 2007, MNRAS, 377, 1795
Cortzen, I., Garrett, J., Magdis, G., et al. 2019, MNRAS, 482, 1618
Davis, T. A., Alatalo, K., Bureau, M., et al. 2013, MNRAS, 429, 534
Davis, T. A., & Bureau, M. 2016, MNRS, 457, 272
Davis, T. A., Greene, J. E., Ma, C.-P., et al. 2019, MNRAS, 486, 1404
Davis, T. A., Young, L. M., Crocker, A. F., et al. 2014, MNRAS, 444, 3427
de Vaucouleurs, G., de Vaucouleurs, A., Corwin, H. G. J., et al. 1991, Third Reference Catalogue of Bright Galaxies (New York: Springer)
den Brok, J. S., Chatzigiannakis, D., Bigiel, F., et al. 2021, MNRAS, 504, 3221
Diamond-Stanic, A. M., & Rieke, G. H. 2010, ApJ, 724, 140
Donoso, E., Yan, L., Tsai, C., et al. 2012, ApJ, 748, 80
Draine, B. T., & Li, A. 2007, ApJ, 657, 810
Gao, Y., & Solomon, P. M. 2004a, ApJS, 152, 63
Gao, Y., & Solomon, P. M. 2004b, ApJ, 606, 271
Gao, Y., Tan, Q.-H., Gao, Y., et al. 2022, ApJ, 940, 133
Gao, Y., Xiao, T., Li, C., et al. 2019, ApJ, 887, 172
Ge, X., Gu, Q.-S., Garcìa-Benito, R., et al. 2021, MNRAS, 507, 4262
Georgakakis, A., Hopkins, A. M., Caulton, A., et al. 2001, MNRAS, 326, 1431
Gong, M., Ostriker, E. C., Kim, C.-G., & Kim, J.-G. 2020, ApJ, 903, 142
Huchra, J. P., Macri, L. M., Masters, K. L., et al. 2012, ApJS, 199, 26
Hudgins, D. M., & Allamandola, L. J. 2005, in IAU Symp. 231, Astrochemistry: Recent Successes and Current Challenges, ed. D. C. Lis, G. A. Blake, & E. Herbst (Cambridge: Cambridge Univ. Press), 443
Hunt, L. K., De Looze, I., Boquien, M., et al. 2019, A&A, 621, A51
Jarrett, T. H., Cohen, M., Masci, F., et al. 2011, ApJ, 735, 112
Jiang, X.-J., Wang, Z., Gu, Q., Wang, J., & Zhang, Z.-Y. 2015, ApJ, 799, 92
Jing, T., & Li, C. 2024, arXiv:2411.08747
Kaneda, H., Onaka, T., Sakon, I., et al. 2008, ApJ, 684, 270
Kauffmann, G., Heckman, T. M., De Lucia, G., et al. 2006, MNRAS, 367, 1394
Kaviraj, S., Schawinski, K., Devriendt, J. E. G., et al. 2007, ApJS, 173, 619
Kelly, B. C. 2007, ApJ, 665, 1489
Kennicutt, R. C. J. 1998, ApJ, 498, 541
Kim, J., Chevance, M., Kruijssen, J. M. D., et al. 2022, MNRAS, 516, 3006
Knapp, G. R., & Rupen, M. P. 1996, ApJ, 460, 271
Koda, J., Sawada, T., Sakamoto, K., et al. 2020, ApJL, 890, L10
Krumholz, M. R., & McKee, C. F. 2005, Apj, 630, 250
Landsman, W. B. 1995, in ASP Conf. Ser. 77, Astronomical Data Analysis Software and Systems IV, ed. R. A. Shaw, H. E. Payne, & J. J. E. Hayes (San Francisco, CA: ASP), 437
Leroy, A. K., Bigiel, F., de Blok, W. J. G., et al. 2012, AJ, 144, 3
Leroy, A. K., Bolatto, A., Gordon, K., et al. 2011, ApJ, 737, 12
Leroy, A. K., Bolatto, A. D., Sandstrom, K., et al. 2023a, ApJL, 944, L10
Leroy, A. K., Rosolowsky, E., Usero, A., et al. 2022, ApJ, 927, 149
Leroy, A. K., Sandstrom, K. M., Lang, D., et al. 2019, ApJS, 244, 24
Leroy, A. K., Sandstrom, K., Rosolowsky, E., et al. 2023b, ApJL, 944, L9
Leroy, A. K., Walter, F., Brinks, E., et al. 2008, AJ, 136, 2782
Leroy, A. K., Walter, F., Sandstrom, K., et al. 2013, AJ, 146, 19
Li, A. 2020, NatAs, 4, 339
Li, C., Kauffmann, G., Fu, J., et al. 2012, MNRAS, 424, 1471
Ma, C.-P., Greene, J. E., McConnell, N., et al. 2014, ApJ, 795, 158
Meijerink, R., & Spaans, M. 2005, A&A, 436, 397
Ocaña Flaquer, B., Leon, S., Combes, F., & Lim, J. 2010, A&A, 518, A9
O'Sullivan, E., Combes, F., Hamer, S., et al. 2015, A&A, 573, A111
O'Sullivan, E., Combes, F., Salomé, P., et al. 2018, A&A, 618, A126
O'Sullivan, E., Forbes, D. A., & Ponman, T. J. 2001, MNRS, 328, 461
Pan, H.-A., Schinnerer, E., Hughes, A., et al. 2022, ApJ, 927, 9
Peng, Y.-j., Lilly, S. J., KovaÄ, K., et al. 2010, ApJ, 721, 193
Rieke, G. H., Wright, G. S., Böker, T., et al. 2015, PASP, 127, 584
Ronayne, K., Papovich, C., Yang, G., et al. 2024, ApJ, 970, 61
Sage, L. J., Welch, G. A., & Young, L. M. 2007, ApJ, 657, 232
Saintonge, A., & Catinella, B. 2022, ARA&A, 60, 319
Sakamoto, S., Hayashi, M., Hasegawa, T., Handa, T., & Oka, T. 1994, ApJ, 425, 641
Salpeter, E. E. 1955, ApJ, 121, 161
Sanders, D. B., & Mirabel, I. F. 1996, ARA&A, 34, 749
Sandstrom, K. M., Bolatto, A. D., Draine, B. T., Bot, C., & Stanimirović, S. 2010, ApJ, 715, 701
Sandstrom, K. M., Bolatto, A. D., Bot, C., et al. 2012, ApJ, 744, 20
Sandstrom, K. M., Koch, E. W., Leroy, A. K., et al. 2023, ApJL, 944, L8
Shivaei, I., & Boogaard, L. A. 2024, A&A, 691, L2
Smith, J. D. T., Draine, B. T., Dale, D. A., et al. 2007, ApJ, 656, 770
Solomon, P. M., Rivolo, A. R., Barrett, J., & Yahil, A. 1987, ApJ, 319, 730
Tacconi, L. J., Genzel, R., & Sternberg, A. 2020, ARA&A, 58, 157
Temi, P., Brighenti, F., & Mathews, W. G. 2009, ApJ, 695, 1
Tielens, A. G. G. M. 2008, ARA&A, 46, 289
Villaume, A., Conroy, C., & Johnson, B. D. 2015, ApJ, 806, 82
Visser, R., van Dishoeck, E. F., & Black, J. H. 2009, A&A, 503, 323
Walterbos, R. A. M., & Schwering, P. B. W. 1987, A&A, 180, 27
Wang, E., Kong, X., & Pan, Z. 2018a, ApJ, 865, 49
Wang, E., Li, C., Xiao, T., et al. 2018b, ApJ, 856, 137
Wang, E., Lilly, S. J., Pezzulli, G., & Matthee, J. 2019, ApJ, 877, 132
Watson, C., Povich, M. S., Churchwell, E. B., et al. 2008, ApJ, 681, 1341
Welch, G. A., & Sage, L. J. 2003, ApJ, 584, 260
Welch, G. A., Sage, L. J., & Young, L. M. 2010, ApJ, 725, 100
Whitcomb, C. M., Sandstrom, K., Leroy, A., & Smith, J. D. T. 2023, ApJ, 948, 88
Wiklind, T., Combes, F., & Henkel, C. 1995, A&A, 297, 643
WISE Team 2020, AllWISE Atlas (L3a) Coadd Images, IPAC, https://catcopy.ipac.caltech.edu/dois/doi.php?id=10.26131/IRSA153
Wolfire, M. G., Hollenbach, D., & McKee, C. F. 2010, ApJ, 716, 1191
Wolfire, M. G., Vallini, L., & Chevance, M. 2022, ARA&A, 60, 247
Wright, E. L., Eisenhardt, P. R. M., Mainzer, A. K., et al. 2010, AJ, 140, 1868
Yajima, Y., Sorai, K., Miyamoto, Y., et al. 2021, PASJ, 73, 257
Yi, S. K., Yoon, S. J., Kaviraj, S., et al. 2005, ApJL, 619, L111
Young, L. M. 2002, AJ, 124, 788
Young, L. M. 2005, ApJ, 634, 258
Young, L. M., Bureau, M., Davis, T. A., et al. 2011, MNRS, 414, 940
Zhang, L., & Ho, L. C. 2023a, ApJ, 943, 1
Zhang, L., & Ho, L. C. 2023b, ApJ, 943, 60